

Z Pinch Kinetics I - A Particle Perspective: Transitional Magnetization and Cyclotron and Betatron Orbits

Daniel W. Crews,¹ Eric T. Meier,¹ and Uri Shumlak^{1,2}

¹*Zap Energy Inc., Everett, WA 98203, USA*

²*University of Washington, Seattle, WA 98195, USA*

(*Electronic mail: daniel.crews@zap.energy)

(Dated: 12 November 2024)

Single-particle orbits are investigated as the basis of a coherent kinetic theory. Analytic solutions including azimuthal circulation are obtained in elliptic functions, of which ideal cyclotron and betatron motions are limiting solutions. The elliptic modulus depends on a trapping parameter and an axis-encircling to axial-drift kinetic energy ratio. Large trapping parameters limit to guiding-center cyclotron motion, while small trapping parameters describe ideal betatron motion. The analytic solutions inform a separation of phase space into trapped and passing trajectories, with which the Bennett solution is decomposed into cyclotron and betatron distributions. The two partial densities are computed to reveal a transitional magnetization layer the extent of which depends only on an ensemble-averaged trapping parameter, equivalent to: the Budker parameter, the pinch-to-Alfvén current ratio, the Larmor radius parameter squared, the Hall parameter squared, the drift parameter squared, and the Hartmann number squared. The interplay of diamagnetic current and axial betatron flux is clarified through partial current densities, and the radial electric fields of shear flows are observed to influence ion orbits particularly around unity Budker parameter.

I. INTRODUCTION

The Z pinch is a quasineutral plasma filament which conducts current along its axis, thereby confining pressure through its self-induced magnetic field. While Z pinches were one of the first plasma confinement concepts for a fusion reactor due to their simple linear geometry and high density¹, they are susceptible to magnetohydrodynamic (MHD) instabilities that disrupt the current². Historically, Z-pinch experiments have focused on utilizing the unstable Z pinch as a neutron and x-ray source³. Recent years have seen significant progress in stabilizing the Z pinch by the use of sheared flows to mitigate the MHD instabilities⁴. Electron temperatures of multiple keV, measured via optical Thomson scattering⁵, have been observed in flow Z-pinch experiments to be temporally coincident with measurements of neutron emission^{6,7}.

The self-magnetic field of the Z pinch has an associated magnetic null on its axis. Magnetic flux density increases from zero on-axis up to a maximum around the pinch radius. For this reason, particles in a Z pinch display variable magnetization, orbiting around magnetic field lines in the magnetized periphery, orbiting through or about the \hat{z} -axis within the current-dense core, and displaying either kind of motion in-between, depending on particle energy and momentum, within a transitional magnetization layer. Through analysis of single-particle orbits, this article explores and clarifies the transitional magnetization regime of Z-pinch orbits.

Kinetic theory, in which plasma is described statistically by a probability density in phase space known as the distribution function, is fundamental to an understanding of plasma properties outside of the MHD regime. The distribution function is used to calculate observables of a plasma species such as density, temperature, and pressure. Distribution functions are understood using kinetic theory, which studies the transport of particles, momentum, and energy at various degrees of collisionality and trajectory magnetization, but is high-dimensional and challenging to use for large-scale modeling, such as predictive whole device modeling used for fusion energy development⁸. Simpler hydrodynamic models obtained by kinetic-theory-informed closures are used for predictive and interpretive modeling of Z-pinch plasmas. Therefore, plasma kinetics is the starting point for more commonly used plasma models.

The statistical description and single-particle dynamics are complementary approaches to understanding plasma behavior. Prediction of key observables is enabled by the ensemble-averaged statistics of the distribution function, while individual trajectories provide particular details. The dynamical equation for the distribution function unites these two perspectives, determining many-

particle observables from the self-consistent dynamics of many trajectories. As plasma dynamics involves such collective, many-particle motions, a full understanding of kinetic theory therefore necessitates a deep understanding of the various trajectories in a plasma configuration.

This work studies the single-particle orbits for varying degrees of magnetization, while a companion article (“the sequel”) considers the continuum, many-particle description⁹. Specifically, this study investigates and classifies orbits in the Z-pinch configuration using the effective potential energy method. The objective is to understand the conditions when ions are well-magnetized in the self-field of a pinched electric current, as ion magnetization is a fundamental property that has profound implications for collective plasma behavior, transport phenomena, wave propagation, instabilities, and the overall dynamics of plasmas on collisionless timescales.

The magnetized orbit of a particle, known as cyclotron or Larmor motion, consists of a circular or helical trajectory of radius r_L , called the gyroradius, about a magnetic field line. Guiding-center theory, based on adiabatic invariance of the magnetic moment¹⁰, describes the corrections to cyclotron motion in inhomogenous fields with a scale length L large compared to the orbital gyroradius ($r_L \ll L$). Most orbits in plasmas magnetized by external magnetic fields are well-approximated by guiding-center theory. A notable exception occurs for self-magnetized, current-carrying plasmas which are characterized by magnetic nulls where magnetic flux density is zero. Orbits in the vicinity of magnetic nulls are not adequately described by guiding-center theory. Such motions beyond the guiding-center approximation are referred to in the literature as non-Larmor orbits¹¹, large Larmor radius orbits¹², Speiser orbits¹³, or simply betatron orbits¹⁴. Non-Larmor magnetic orbits are of central importance in charged particle beams and particle accelerators¹⁵.

Early studies of electric currents in the magnetosphere and laboratory plasmas identified the importance of magnetic null regions within magnetized plasmas, which were originally known as neutral surfaces¹⁶. These neutral surfaces may separate regions of oppositely directed magnetic fields (thus supporting planar current sheets or X-points) or may be found at the center of current-carrying filaments (for cylindrical current pinches). Such magnetic null surfaces associated with current-carrying self-magnetized plasmas are the source of a multitude of instabilities which are studied under the umbrellas of magnetic reconnection and the stability of current pinches.

An important element in understanding these neutral surfaces is the analysis of single-particle orbits in the vicinity of the magnetic null. Historically, non-Larmor orbits occurring in magnetic reconnection have received the most attention, usually in the context of understanding particle energization by the Earth’s magnetotail. In 1957, E. N. Parker studied orbits around the null point

of planar current sheets, identifying classes of orbits and obtaining some analytic results in elliptic integrals¹⁷. T. W. Speiser (1965), interested in particle energization in the magnetotail, built on Parker's results and considered orbits near the magnetic null in the presence of current-parallel electric fields^{18,19}. B. U. Ö. Sonnerup (1971) notably built on both previous works by analysis of the orbital adiabatic invariants and further developed the results in elliptic integrals²⁰.

An important later work by Büchner and Zelenyi (1989) described orbit energization beyond adiabatic invariance via deterministic chaos and stochasticity²¹. Stochasticity of non-Larmor orbits became recognized as critical for the so-called diffusion region of a reconnecting current sheet²², which subsequently took on a more nuanced perspective as a competition between Fermi and betatron acceleration mechanisms²³, with non-Larmor curvature drifts also found to drive heating²⁴ and scattering²⁵. TenBarge, Juno, and Howes (2024) recently utilized continuum kinetic simulation capabilities to directly study electron energization in reconnection and focused on the way in which non-Larmor orbits control the process²⁶. Beyond heating, non-gyrotropic pressure anisotropy resulting from magnetized pressure-strain interactions has been recognized to play an important role in the reconnection process through the modification of transport coefficients¹¹. A. J. Brizard (2017) built on the earlier work of Parker, Sonnerup, and others by presenting a solution in elliptic functions for trajectories in a linearly varying magnetic field, with the motivation of studying the applicability of guiding-center theory²⁷.

Single-particle orbits in the area of current pinches has its origin in the Alfvén current limit²⁸ (1939), beyond which a stream of non-neutralized electrons turns around in its self-field. W. H. Bennett (1934) determined the kinetic equilibrium and the well-known Bennett pinch profiles occurring in quasi-thermal equilibrium, but did not consider orbits²⁹. In summarizing the Bennett pinch, O. Buneman (1961) noted that particle orbits could be found in principle but did not go farther than describing the method of invariants³⁰. P. Gratreau (1978) made a comprehensive analysis of pinch orbits while describing a class of generalized Bennett equilibria. M. G. Haines (1978) explained how “singular orbits” about the magnetic axis (Sonnerup's “meandering orbits”) displayed an ion flux from anode to cathode (in the absence of bulk ion velocity) cancelled by an oppositely directed diamagnetic current³¹. Haines emphasized the importance of betatron-type ion orbits throughout his career, utilizing them to theoretically explain the formation of ion beams in $m = 0$ instabilities, among other aspects of Z-pinch physics^{32–34}. As a type of self-field current pinch, betatron-type orbits also play a key role in field-reversed configuration (FRC) plasmas³⁵. Indeed, the FRC s-parameter, which measures the fraction of ion betatron orbits, plays the same role for

FRCs as the Budker parameter determined in the present work for Z pinches; both are linked to the ratio of ion Larmor radius to plasma size.

Notable contributions of this work to the study of magnetically self-focused plasmas include:

- Demonstration of the equivalence between Speiser orbits and axis-crossing betatrons of the pinch, unifying reconnection and pinch orbit theories (Section II D),
- Development of complete analytic orbital solutions including azimuthal circulation, parametrized by a magnetic trapping parameter and kinetic energy anisotropy (Section II G),
- Formulation of a generic trapping criterion including axis-encircling motion (Section II G 2),
- Characterization of the betatron/cyclotron phase-space boundary (Section III A),
- Novel division of the canonical distribution into trapped and passing orbits (Section III B),
- Observation of a transitional layer between trapped and passing orbits (Section III C),
- Demonstration that the location and thickness of the transitional magnetization layer depends only on the Budker parameter (Section III D), and its equivalence with:
 - an ensemble-averaged magnetic trapping parameter,
 - the finite Larmor radius (FLR) parameter (squared),
 - the characteristic Hall parameter (squared),
 - the Alfvén current scale,
 - the characteristic Hartmann number (squared),
 - and the inverse drift parameter (squared).
- Discussion of counter-balancing betatron fluxes and diamagnetic fluxes (Section III E). The flow pinch orientation $\mathbf{j} \cdot \mathbf{v} < 0$ is observed to reduce the laboratory-frame ion betatron flux.

These results are progressively developed from the orbital solutions in Section II, by fixing the electric fields and the frame of reference in Section II A, followed by a description of the effective potential method in Section II B and a high-level description of orbits in Section II C. The properties of orbits are studied analytically, first for axis-crossing trajectories without angular momentum in Section II D and later for non-zero angular momentum in Section II G. Section III, informed by the analytic orbits, proposes a novel splitting of the distribution function based on its degree of magnetization and averages this splitting over the kinetic equilibrium distribution of the Bennett pinch. Finally, Section IV considers the influence of radial electric fields in radially sheared axial flows on the degree of orbit magnetization.

The analytic properties of these orbits are applied in the sequel, which progressively treats

Z-pinch kinetic theory topics from the continuum perspective⁹. The sequel discusses several topics mentioned in the historical survey above, specialized for the sheared-flow Z pinch: adiabatic and doubly adiabatic compression, anisotropy production, kinetic equilibrium of sheared flows, the magnetized pressure-strain interaction, and consequences of gyroviscosity in a magnetic field such as the self-organization and self-generation of flows. The discussion of collisionless adiabatic compression of a Z pinch utilizes the adiabatic invariants of betatron orbits (similar to Sonnerup’s analysis²⁰), drawing heavily on the results obtained in this work.

II. ORBIT MAGNETIZATION IN THE Z PINCH

We begin by studying orbits in the Z pinch and their degree of magnetization. The main tool utilized is the effective potential method, which provides a qualitative understanding of orbits for general pinch profiles. Exact solutions are obtained in the particular case of motion in the self-magnetic field of a uniform current density, enabling an analytic study of the orbits. Such a classification provides insights into phase space dynamics, informs a high-level classification of orbits, and delineates the boundaries of validity for reduced models such as gyrokinetics.

Asymptotically, a clear distinction can be made between the various types of orbits in a Z pinch. That is, the analytic orbits obtained in this section possess two parameters; a magnetization parameter and a ratio of field-parallel to field-perpendicular energies. From the asymptotic limits of these parameters we distinguish ideal particle motions which we classify as well-magnetized (“cyclotron”) or non-magnetized (“betatron”) trajectories. Particles in these two classes of trajectories display distinct cyclotron and betatron frequencies. The betatron orbital frequency characterizes both radial bounce motions and axis-encircling azimuthal motions. Cyclotron orbits may be considered as the “well-magnetized” orbits because the adiabatic invariant associated with their radial motion is precisely the magnetic moment, and are thus well-described by the guiding-center theory. Betatron orbits have a distinct adiabatic invariant associated with their radial bounce motion, and thereby are not governed by standard guiding-center theory.

A. Radial electric field and the center-of-charge frame

Before employing the effective potential method, we first fix the frame of reference and the apparent electromagnetic fields. In the present scenario, we consider the ideal Z-pinch configuration,

an axisymmetric field in the cylindrical configuration space coordinates (r, θ, z) consisting of an axially directed magnetic vector potential $\mathbf{A} = A_z(r)\hat{z}$ self-consistently sustained by an axial current density $\mathbf{j} = j_z(r)\hat{z}$ supporting an azimuthal magnetic field $\mathbf{B} = -\frac{dA_z}{dr}\hat{\theta}$. In the magneto-quasistatic (MQS) limit of the Lorentz transformation, a flow Z pinch of axial fluid velocity $\mathbf{v} = v_z\hat{z}$ in the lab frame is associated with a radial electric field of voltage $\phi = -\mathbf{v} \cdot \mathbf{A} = v_z\psi'_\theta$ where $\psi'_\theta = \int_0^r B_\theta dr'$ is the azimuthal magnetic flux per unit length.

In a two-species electron-ion plasma with $Z_i = 1$ there is a unique Lorentz frame of reference in which $E_r = 0$ and the quasineutral pinch plasma is perfectly neutral³⁶. Equilibrium is frame-invariant; if the plasma is in equilibrium in one frame then it must be in equilibrium in every frame. In the ion frame, static ion pressure is confined through a radially inward electric field while electron equilibrium is provided by an inward magnetic force balancing electron pressure plus the repulsive electric field, and vice versa in the electron frame where the electric field is radially outward. There is an intermediate frame in which both electrons and ions are confined by a purely magnetic force, and no electric field is observed. This frame is characterized by perfectly counterstreaming ions and electrons, and is called the center-of-charge frame (in analogy to center-of-mass velocity) or the perfectly neutral Lorentz frame. The motional electric field of radially uniform motion can therefore be transformed away for the purpose of trajectory analysis, but radially sheared axial flows produce E_r that cannot be transformed away.

To demonstrate the above, consider the MQS Lorentz transformation,

$$\mathbf{E}' + \mathbf{v}' \times \mathbf{B} = \mathbf{E} + \mathbf{v} \times \mathbf{B} \quad (1)$$

with a frame-change $\mathbf{v} \rightarrow \mathbf{v}'$, while $\mathbf{B}' = \mathbf{B}$. Let the velocity \mathbf{v} be the ion velocity of the frames, $\mathbf{v}' = \mathbf{v}_i$. In the ion rest frame where $\mathbf{v}' = 0$, an electric field balances the ion pressure gradient as $\mathbf{E}_{\text{ion frame}} = \frac{1}{ne}\nabla p_i$, while in the electron rest frame where $\mathbf{v}' = \mathbf{v}_\ell - \mathbf{j}/ne$ (\mathbf{v}_ℓ being lab frame ion velocity) the electric field balances electron pressure as $\mathbf{E}_{\text{electron frame}} = -\frac{1}{ne}\nabla p_e$. Then, seeking the frame where $\mathbf{E}' = 0$ we find $\mathbf{v}' = \mathbf{v}_\ell - \mathbf{j}/2ne$ provided that $\nabla(p_e + p_i) = \mathbf{j} \times \mathbf{B}$ and $p_e = p_i$. The velocity $\mathbf{v}_c \equiv \mathbf{v}_\ell - \mathbf{j}/2ne$ describes the transformation between lab frame and center-of-charge frame velocities.

Radially sheared axial flows induce motional electric fields which do not transform away in the center-of-charge frame. A particular radial electric field profile has a special significance, namely the electric field arising from a critical axial flow profile for which collisionless viscous shear stress production is zero. The phenomenon of steady collisionless shear flow is related to the magnetized

pressure-strain interaction and thermal anisotropy, both of which are discussed in the sequel⁹. This critical flow profile occurs when the plasma velocity of a Bennett equilibrium is a linear function of magnetic flux,

$$v_{z,i} = u_d/2 + \gamma \frac{q_i \psi'_\theta}{m_i} \quad (2)$$

with γ a constant and $u_d = v_i - v_e = j/ne$ the relative drift velocity. The electric potential energy associated with the flow of Eq. 2 is

$$q_i \phi = -\gamma \frac{(q_i A_z)^2}{2m_i}. \quad (3)$$

Equation 3 is arrived at from Eq. 2 by observing that in a Bennett equilibrium observed from the center-of-charge frame, the pressure gradient is completely balanced by magnetic forces and therefore the remaining electromagnetic force balances to zero. Therefore, the field in the center-of-charge frame satisfies $\mathbf{E} = -(\mathbf{v} - \mathbf{u}_d/2) \times \mathbf{B}$. As $B_\theta = \frac{d\psi'_\theta}{dr}$ and $\mathbf{E} = -\nabla\phi$, one has

$$\frac{d\phi}{dr} = -\gamma \frac{q_i \psi'_\theta}{m_i} \frac{d\psi'_\theta}{dr} = -\gamma \frac{q_i}{2m_i} \frac{d\psi_\theta^2}{dr} \quad (4)$$

from which Eq. 3 is recovered. The critical shear flow voltage is quadratic in the flux (termed critical as it represents the balance point of internal stresses, discussed in the sequel). The potential energy of a radially sheared axial flow therefore influences particle motion in a way that cannot be transformed away. The influence of radial electric fields on the conclusions of this work are considered in Section IV.

B. Effective potential energy method for the Z pinch

The concept of potential momentum, fundamental to magnetic confinement, is commonly utilized to construct the Hamiltonian of a particle interacting with a magnetic field³⁷. The exchange of potential and kinetic momentum is usually simplified into an effective potential energy function describing the particle's motion within the magnetic field, allowing the application of well-known energy methods³⁸. This effective potential method is often employed to analyze particle motion in charged particle beams influenced by both external and self-generated magnetic fields³⁹⁻⁴¹.

The effective potential energy function is arrived at by considering the invariants of motion for a particle of species α with mass m_α and charge q_α . Particle motion in the Z pinch is characterized by three conserved quantities: kinetic energy $H = \frac{1}{2}m_\alpha v_\alpha^2$, axial momentum $P_z = m_\alpha v_z + q_\alpha A_z$, and angular momentum $L_\theta = m_\alpha v_\theta r$, where the particle's velocity vector is expressed as $\vec{v}_\alpha =$

$v_r \hat{r} + v_\theta \hat{\theta} + v_z \hat{z}$ (distinct from the fluid ion velocity \mathbf{v} in the previous section) in cylindrical coordinates. The three constants of motion are

$$H = \frac{1}{2}m_\alpha v_r^2 + \frac{1}{2}m_\alpha v_\theta^2 + \frac{1}{2}m_\alpha v_z^2, \quad (5a)$$

$$P_z = m_\alpha v_z + q_\alpha A_z, \quad (5b)$$

$$L_\theta = m_\alpha v_\theta r. \quad (5c)$$

Field-particle coupling is described by Eq. 5b which states that when a charge changes radial position, its kinetic momentum is transformed into magnetic potential momentum and vice versa. Substituting Eqs. 5b and 5c into Eq. 5a eliminates the velocities v_θ and v_z , yielding a reduced one-dimensional description of motion,

$$H = K_r + U(r; P_z, L_\theta), \quad (6)$$

$$U(r; P_z, L_\theta) \equiv \frac{(P_z - q_\alpha A_z(r))^2}{2m_\alpha} + \frac{1}{2m_\alpha} \left(\frac{L_\theta}{r} \right)^2, \quad (7)$$

where $K_r \equiv \frac{1}{2}m_\alpha v_r^2$ is the radial kinetic energy and $U = K_z + K_\theta$ the effective potential energy, which is made up of the axial and azimuthal kinetic energies as functions of the constants of motion and of position. Equation 6 describes the reduced radial motion in a two-parameter family of effective potential wells $U = U(r; P_z, L_\theta)$, parametrized by the particular momentum levels P_z and L_θ . The varying sum of axial and azimuthal kinetic energies along a trajectory acts as an effective potential energy for the radial motion because the magnetic Lorentz force does no work.

Figure 1 illustrates profiles of magnetic vector potential and current density for typical Z-pinch configurations. The dashed lines correspond to a uniform current density, and the solid lines to a Bennett pinch where $j_z = j_0(1 + (r/r_p)^2)^{-2}$, with r_p the characteristic radius and j_0 the on-axis current density. The radial profile of vector potential (*viz.* azimuthal magnetic flux) controls particle motion for a given set of invariants through the effective potential energy function Eq. 7. The axial velocity is directly controlled by the distribution of vector potential, which is easily understood when \mathbf{A} is interpreted as a potential momentum field.

C. Betatron and cyclotron-type trajectories

The effective potential method for the magnetic well described in Section II B enables particle trajectories to be distinguished by their integrable motions in phase space and categorized according to their energy levels. In the case of the ideal Z pinch, the highest-level distinction is between

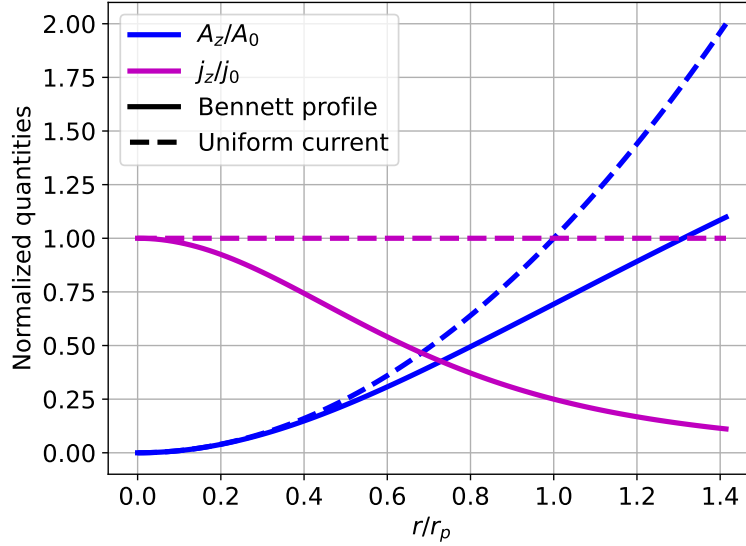


FIG. 1. Magnetic vector potential (in blue) and axial current density (in purple) are shown for constant axial current density (dashed lines) and for a Bennett pinch profile (solid lines). Note that the characteristic magnetic vector potential $A_0 < 0$ for everywhere positive current density $j_z > 0$, such that $A_z/A_0 > 0$. The vector potential profile acts as a magnetic well for charged particles in the specific sense of Eq. 7. For the Bennett pinch $A_z = -\frac{\mu_0 I}{4\pi} \ln(1 + (r/r_p)^2)$ where I is the total pinch current and r_p the characteristic plasma radius, which expands about the magnetic axis as $A_z = -\frac{\mu_0 I}{\pi r_p^2} \frac{r^2}{4} + \mathcal{O}(r^4)$, the first term corresponding to the uniform current density considered for the analytic solutions presented in Sections II D and II G.

the cyclotron and betatron-type trajectories. The distinction rests on both the local magnetic field magnitude and the particle energy level. Essentially, cyclotron-type trajectories have a sufficiently low kinetic momentum relative to the local magnetic flux to be magnetically localized. The higher momentum betatron-type trajectories are delocalized in the sense that they have access to a larger phase space volume than the cyclotrons. As the distinction depends on both the magnetic field structure and the trajectory constants, then given a distribution function across all energy, any given radial location will have some cyclotron particles and some betatron particles. The relative populations of cyclotron and betatron-type trajectories are further explored in Section III.

Betatron and cyclotron-type trajectories are most clearly distinguished in the special case of zero angular momentum ($L_\theta = 0$) about the magnetic axis, in which case Eq. 7 is

$$U(r; P_z) = \frac{(P_z - q\alpha A_z)^2}{2m_\alpha}. \quad (8)$$

Equation 8 represents a single-parameter family of potential wells. Such wells satisfy $U \geq 0$ and

are either of a single-well or double-well type for monotonic $A_z(r)$. For a positive charge in a well sustained by $+z$ -directed electric current⁴², Eq. 8 is of the double-well type for $P_z < 0$ with $U_{\min} = 0$ where $P_z = q\alpha A_z$ (representing, in the lab frame, static charges), and of single-well type for $P_z > 0$. The classification is opposite in the sign of P_z for negatively charged particles. Essentially, cyclotrons occupy energy levels within the double-well minimum with $P_z < 0$ while betatrons either have $P_z > 0$ or occupy energy levels above the double-well barrier.

In practical terms, cyclotrons are magnetized charges for which standard guiding-center theory is reasonably applicable. On the other hand, betatrons are magnetically trapped but “unmagnetized” particles, where “unmagnetized” in the presence of a magnetic field means that the particles execute non-Larmor orbits ranging from axis-encircling helical trajectories to axis-crossing radial bounce motions to drifting figure-eight type orbits. These non-Larmor motions are termed betatron motions as their characteristic frequency is a non-Larmor magnetic frequency known as the betatron frequency. A systematic exploration of this transitional magnetization regime linking these various motions constitutes a significant contribution of this work.

1. *Linear betatrons and guiding-center cyclotrons*

Generically, particle trajectories in the Z-pinch field display nonlinear oscillations, but asymptotically some particles execute linear oscillations. Figure 2 shows linear betatron and cyclotron-type trajectories in trajectories (a-c), which we summarize in this section, in addition to characteristic figure-eight-type nonlinear betatron orbits which are useful to keep in mind for later. Linear betatrons execute simple harmonic motion about the magnetic axis of an axial current at a characteristic frequency called the betatron frequency ω_β . We consider two kinds of linear betatrons, the “helical” (Fig. 2b) and “axis-crossing” (Fig. 2c) types.

Considering first the helical betatron, suppose an ion is in radial equilibrium due to an inward Lorentz force $q_i v_z B_\theta$ from current-aligned axial velocity and an outward centrifugal force $m_i \omega^2 r$ resulting from an orbit at radius r about the \hat{z} -axis with angular velocity $\omega = v_\theta / r$. In equilibrium, the orbital angular frequency is

$$\omega_\beta^2 = \omega_{ci} \frac{v_z}{r} \quad (9)$$

where $\omega_{ci} = \frac{q_i B_\theta}{m_i}$ is the ion cyclotron frequency. In the beam limit of small self-fields (Section III D), the assumption that all particles execute helical orbits is the basis of a solvable dispersion relation for hose instabilities⁴³ (a type of beam kink instability). The ideal helical betatron constitutes

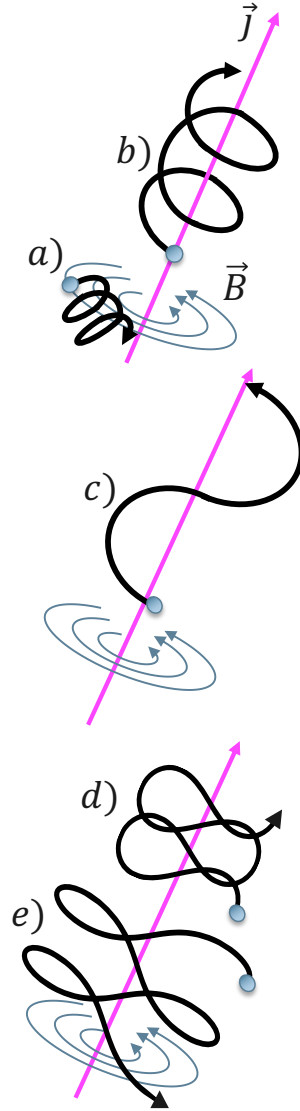


FIG. 2. The two kinds of idealized orbits in a Z pinch are the cyclotron and betatron oscillations. In reality, particle trajectories fill a broad spectrum between ideal cyclotron and betatron motions. Here, the magnetic axis is depicted as the purple line carrying a current j , and the magnetic field lines surrounding the current are depicted as the vector field B . Positively charged ion trajectories are illustrated in black lines for cyclotron (a) and betatron (b,c,d,e) motions. A helical axis-encircling betatron orbit is shown in trajectory (b), and axis-crossing betatron orbits are depicted in trajectories (c,d,e) of linear and nonlinear types. Cyclotrons ∇B -drift opposite their species bulk velocity unless their field-parallel energy exceeds twice their field-perpendicular energy, $K_{\parallel} > 2K_{\perp}$. Most betatrons drift parallel to the direction of their species bulk velocity (for ions, in the direction of j) as in trajectories (c,d), but some drift counter the bulk velocity as in trajectory (e). Section II F shows that forward-drifting and backward-drifting betatrons are separated by a critical value of the magnetic trapping parameter satisfying a transcendental equation.

pure curvature drift motion, occupies the ground state of the effective potential for radial motion, and consequently has zero radial action. Given some energy level, whether the radial action is identifiable with the magnetic moment, and consequently whether the drift motion is Larmor or not, depends on the particle's trapping parameter and ratio of perpendicular-to-parallel energies (explored in Section II G 2).

The axis-crossing linear betatron is found only asymptotically in the limit of high momentum P_z with approximately constant axial velocity⁴⁴. The betatron bounces radially in simple harmonic motion with a characteristic frequency again given by Eq. 9, where r is the bounce amplitude. Thus, the form of Eq. 9 may be understood as the characteristic betatron frequency.

Ideal cyclotron motion has the characteristic frequency $\omega_{c\alpha} = q_\alpha B / m_\alpha$ and excursion (Larmor) radius $r_L = v_\perp / \omega_c$. Note that Eq. 9 reduces to the cyclotron frequency when r is the gyroradius. The first-order correction to cyclotron motion is provided by guiding-center theory (expanded asymptotically in the small Larmor radius regime, or equivalently in the trapping parameter as considered in the following), in which the axial drift velocity is the sum of the ∇B and curvature drifts. The validity of the guiding-center approximation to Z-pinch orbits is studied in the Sections II D and II G and found to describe well most of the ion cyclotron trajectories. However, standard guiding-center theory does not apply to any of the betatron ions, which all sample the transitional magnetization regime. A relevant question is what parameters govern the relative fractions of cyclotron and betatron orbits in a Z pinch, and this is answered in Section III.

D. Analytic solution with zero angular momentum

Figure 3 illustrates the cyclotron-betatron distinction by plotting the effective potential and trajectory of a positive ion in a Z-pinch magnetic well in the case of a uniform current density for which the magnetic vector potential is quadratic. A qualitative distinction can be seen between low and high energy orbits in terms of their excursions from the radial equilibrium point where $U = U_{\min}$. For zero angular momentum $L_\theta = 0$, the quadratic magnetic vector potential leads to a quartic effective potential, which is known to be exactly solvable in terms of elliptic functions⁴⁵. The case $L_\theta \neq 0$ is also exactly solvable, and this is done in Section II G. We present these analytic orbital solutions in terms of their energy and momentum constants H , P_z and compare to the guiding-center approximation for both the cyclotron²⁷ and betatron-type particles.

Having assumed $L_\theta = 0$, Cartesian coordinates (x, y) are introduced, and $y = 0$ is taken in order to

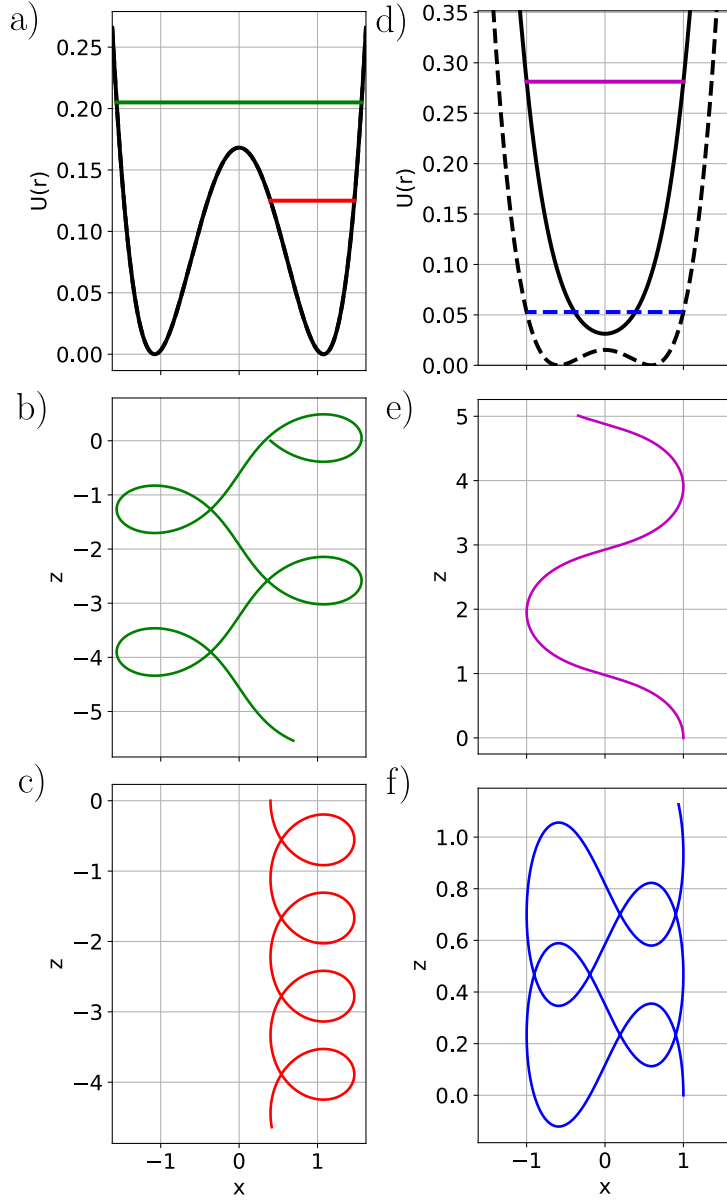


FIG. 3. Effective potential energy function $U = U(r; P_z)$ (with $r = \sqrt{x^2 + y^2}$ plotted for $y = 0$) and drift orbits of ions with zero angular momentum for dimensionless dynamics in a magnetic vector potential $A_z = -r^2/2$, showing (a-c) backward-drifting orbits of cyclotron type (red) and axis-crossing betatron type (green), and (d-f) current-aligned betatron orbits of figure-eight type (blue) and radial-bounce type (magenta). The orbits of (a-c) share the same value of canonical momentum $P_z = -0.58$. The cyclotron orbits trap within the double well with low energies $H < P_z^2/2m_\alpha$, while the betatron orbits are high energy $H \geq P_z^2/2m_\alpha$, being magnetically trapped but not localized. Both forward- and backward-drifting figure-eight betatron orbits have $P_z < 0$ and $H \geq P_z^2/2m_\alpha$, while the radial-bounce orbit has $P_z > 0$, oscillating within a quartic single-well.

work in the (x, z) -plane. Vector component subscripts are now omitted. The magnetic field is taken to be $\mathbf{B} = B_0(x/L)\hat{\theta}$. Dimensions are normalized as length to L , time to ω_{c0}^{-1} with $\omega_{c0} \equiv q\alpha B_0/m\alpha$, velocity to $v_0 \equiv L\omega_{c0}$, momentum to $m\alpha v_0$, energy to $m\alpha v_0^2$, and magnetic potential to B_0L . In the normalized coordinates Eq. 6 rearranges to

$$e^2 = \dot{x}^2 + (P - A)^2 \quad (10)$$

$$\implies \dot{x}^2 = (e - (P - A))(e + (P - A)) \quad (11)$$

where $e^2 \equiv 2H$ and P, A are the normalized axial momentum and magnetic potential. A normal form of Eq. 11 is obtained by, taking $e = +\sqrt{2H}$, defining $\tilde{x} \equiv x/\sqrt{2(e - P)}$, $\tilde{t} \equiv \sqrt{e}t$, and $\tilde{A} \equiv A/(e - P)$, as well as a parameter $\alpha \equiv (e - P)/2e$. The branch $e = +\sqrt{2H}$ keeps $\alpha \geq 0$, producing

$$\left(\frac{d\tilde{x}}{d\tilde{t}}\right)^2 = (1 + \tilde{A})(1 - \alpha(1 + \tilde{A})). \quad (12)$$

We focus on $\alpha \geq 0$ to glean physical intuition without many solution branches; the case $\alpha < 0$ is included in the complete solution with arbitrary L_θ in Section II G. For the quadratic potential $A = -x^2/2 \implies \tilde{A} = -\tilde{x}^2$, Eq. 12 is

$$\left(\frac{d\tilde{x}}{d\tilde{t}}\right)^2 = (1 - \tilde{x}^2)(1 - \alpha(1 - \tilde{x}^2)). \quad (13)$$

The solution of Eq. 13 with initial conditions $x(0) = x_0$ and $\dot{x}(0) = 0$ can be expressed with the Jacobi elliptic functions⁴⁵,

$$x(t) = \begin{cases} x_0 \operatorname{cn}(\sqrt{e}t | \alpha) & 0 < \alpha < 1, \\ x_0 \operatorname{dn}(\sqrt{e\alpha}t | \alpha^{-1}) & \alpha > 1, \end{cases} \quad (14)$$

where the case $\alpha > 1$ is determined by Jacobi's parameter transformation⁴⁶ from $\operatorname{cn} \rightarrow \operatorname{dn}$. As discussed below, $0 < \alpha < 1$ corresponds to the betatrons and $\alpha > 1$ to the cyclotrons. The radial velocities are found by differentiation of Eq. 14,

$$\dot{x}(t) = \begin{cases} c_1 \operatorname{sn}(\sqrt{e}t | \alpha) \operatorname{dn}(\sqrt{e}t | \alpha) & 0 < \alpha < 1, \\ c_2 \operatorname{sn}(\sqrt{e\alpha}t | \alpha^{-1}) \operatorname{cn}(\sqrt{e\alpha}t | \alpha^{-1}) & \alpha > 1 \end{cases} \quad (15)$$

with $c_1 \equiv -x_0\sqrt{e}$ and $c_2 \equiv -x_0\sqrt{e/\alpha}$, and the axial velocity is found by rearranging $P = \dot{z} + A = \dot{z} - x^2/2$ into

$$\dot{z}(t) = \begin{cases} \dot{z}_0 + A_0 \operatorname{sn}^2(\sqrt{e}t | \alpha) & 0 < \alpha < 1, \\ \dot{z}_0 + A_0 \alpha^{-1} \operatorname{sn}^2(\sqrt{e\alpha}t | \alpha^{-1}) & \alpha > 1 \end{cases} \quad (16)$$

where $\dot{z}(0) = \dot{z}_0$ is the initial axial velocity of the particle and $A_0 = -x_0^2/2$ its initial potential momentum. Time integration of Eq. 16 yields the axial position (taking $z_0 = 0$),

$$z(t) = \begin{cases} Pt - A_0 \frac{\mathcal{E}(\sqrt{et}|\alpha) - (1-\alpha)\sqrt{et}}{\sqrt{e\alpha}} & 0 < \alpha < 1, \\ Pt - A_0 \frac{\mathcal{E}(\sqrt{e\alpha t}|\alpha^{-1})}{\sqrt{e\alpha}} & \alpha > 1 \end{cases} \quad (17)$$

where $\mathcal{E}(x|\alpha) \equiv E(\text{am}(x|\alpha)|\alpha)$ is Jacobi's epsilon function⁴⁶, *i.e.* the second incomplete elliptic integral $E(x|\alpha)$ evaluated at the elliptic amplitude $\text{am}(x|\alpha)$. Lastly, the exact nonlinear radial oscillation periods are determined as

$$T(\alpha) = \begin{cases} 4K(\alpha)/\sqrt{e} & 0 < \alpha < 1, \\ 2K(\alpha^{-1})/\sqrt{e\alpha} & \alpha > 1 \end{cases} \quad (18)$$

with $K(\alpha)$ the first complete elliptic integral. Equation 18 limits as $T(0) = 2\pi/\sqrt{e}$, $\lim_{\alpha \rightarrow \infty} T \rightarrow 2\pi/x_0$, and $\lim_{\alpha \rightarrow 1} T \rightarrow \infty$ on the separatrix. Case $\alpha \rightarrow 0$ is the harmonic betatron period and $\alpha \rightarrow \infty$ the harmonic cyclotron period (because normalized $B_\theta = x$). The motion is simply harmonic at both $\alpha \rightarrow 0$ and $\alpha \rightarrow \infty$, separated at $\alpha = 1$ by an infinite-period separatrix.

E. The magnetic trapping parameter and relation to the Larmor radius parameter

The quantity $\alpha \equiv (e - P)/2e$ of Section IID has a clear physical interpretation as a magnetic trapping parameter. That is, given the chosen initial conditions, $2H_0 = \dot{z}_0^2 \implies e = |\dot{z}_0|$ and $P = \dot{z}_0 + A_0$ such that $e - P = -A_0$. Restoring units,

$$\alpha = -\frac{1}{2} \frac{q_\alpha A_0}{m_\alpha v_{z0}} \quad (19)$$

where the previous solutions are valid provided $\alpha > 0$, this occurring for $q_\alpha > 0$ with $v_{z0} > 0$ because $A_0 < 0$. The general solution for arbitrary α and L_θ is presented in Section IIG. Thus, the modulus quantifying the spectrum from betatron to cyclotron oscillation is half the ratio of the two components of the canonical momentum P_z . Magnetic potential momentum dominates kinetic momentum for well-magnetized particles, and vice-versa. The trapping parameter (Eq. 19) often arises in magnetic trapping analysis⁴¹. For a linearly varying magnetic field (constant j_z), the trapping parameter is also the ratio of gradient length scale ($B/\nabla B = r$) to Larmor radius ($r_L = v_z/\omega_c$),

$$\alpha = \frac{1}{4} \frac{r}{r_L} \quad (20)$$

and hence expansions in the trapping parameter coincide with those in the inverse Larmor radius.

F. Orbit excursion, orbit-averaged drift, and the guiding-center approximation

Here, the applicability of the guiding-center approximation is considered for the orbits of the Z pinch. The orbital excursion radius is studied, and orbit-averaged axial drift velocities are computed using the analytic expression of the oscillation periods in terms of complete elliptic integrals of Section II D. These considerations enable a comparison to the predictions of guiding-center theory. As expected, the cyclotron drift velocity is found to be well-represented by the guiding-center ∇B drift velocity $\hat{z} \cdot \mathbf{v}_{\nabla B} = \mu \nabla B / B^2$ where μ is the magnetic moment²⁷, while the betatron drift velocity is not.

The ratio of the exact orbit-averaged excursion to the expected Larmor radius is calculated for cyclotrons as

$$\frac{\langle x \rangle - x_0}{r_L} = 4\alpha \left(1 - \frac{\pi}{2K(\alpha^{-1})} \right), \quad \alpha > 1 \quad (21)$$

where the first-order Larmor radius r_L is related to the initial position and the trapping parameter by $x_0 = 4\alpha r_L$ (Eq. 20). The expression in Eq. 21, plotted in Fig. 4, limits to unity as $\alpha \rightarrow \infty$ and to 4 as $\alpha \rightarrow 1$. That is, expanding Eq. 21 for $\alpha \gg 1$ gives the first-order correction in the trapping parameter,

$$\frac{\langle x \rangle - x_0}{r_L} = 1 + \frac{5}{4} \left(\frac{1}{4\alpha} \right) + \mathcal{O}(\alpha^{-2}) \quad (22)$$

As expected, Eq. 22 agrees with the established formula for the guiding center displacement in a magnetic gradient to first-order in the trapping parameter⁴⁷. To determine the orbit-averaged axial velocity, note that the quarter-period averaged elliptic sine squared is

$$\frac{1}{K(\alpha)} \int_0^{K(\alpha)} \text{sn}^2(t|\alpha) dt = \frac{1}{\alpha} \left(1 - \frac{E(\alpha)}{K(\alpha)} \right) \quad (23)$$

with $E(\alpha)$ the second complete elliptic integral. The orbit-averaged axial velocity is found to be

$$\langle \dot{z} \rangle = P - A_0 \begin{cases} \frac{E(\alpha) - (1-\alpha)K(\alpha)}{\alpha K(\alpha)} & 0 \leq \alpha < 1, \\ \frac{E(\alpha^{-1})}{K(\alpha^{-1})} & \alpha > 1 \end{cases} \quad (24)$$

Two cases of interest following from Eq. 24 are the expected axial velocities of cyclotrons and betatrons. The cyclotrons undergo the small radius guiding-center drift, in this case the ∇B drift, to leading order in the trapping parameter. That is, expanding Eq. 24 for $\alpha \gg 1$ gives $\langle \dot{z} \rangle = -e^2 / 2x_0^2 + \mathcal{O}(\alpha^{-4})$ such that $\langle \dot{z} \rangle \approx -H \nabla B / B^2$ to leading-order in the trapping parameter, producing the expected guiding-center ∇B drift. Section II G recovers the curvature drift for $\alpha \gg 1$ including azimuthal velocities.

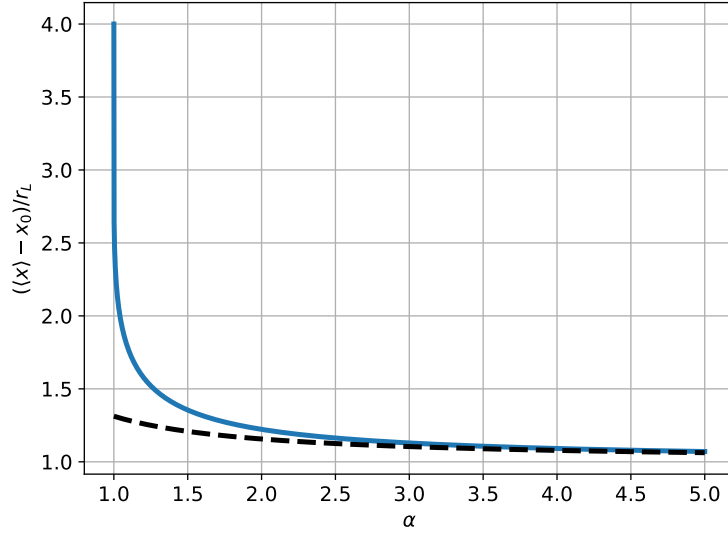


FIG. 4. Departure of the orbital excursion radius from the Larmor radius with the trapping parameter $\alpha \equiv -q\alpha A_{z0}/2m_\alpha v_{z0}$ shown in terms of the analytic solution (solid line) and the leading-order, guiding-center correction in α (dashed line). The limit $\alpha \rightarrow \infty$ approaches ideal cyclotron motion while $\alpha \rightarrow 1$ approaches the cyclotron-betatron separatrix. Leading-order guiding-center theory satisfactorily predicts the displacement for $\alpha \geq 2$.

Linear, harmonic betatron motion (as depicted in Fig. 2c) occurs in the small trapping parameter limit, $\alpha \rightarrow 0^+$. It is necessary to consider distinctly the limits of small positive and negative trapping parameters because the corresponding untrapped orbits are distinct (explored in Section II G). With $\alpha \geq 0$, setting $\alpha = 0$ gives the orbit-averaged betatron velocity as $\langle \dot{z} \rangle = (e + P)/2$. The harmonic betatron velocity is positive (aligned with the current) because their energy is at least $P_z^2/2m_\alpha$, thus $2H > P^2 \implies e + P > 0$, and their particular velocity depends on their energy level. Linear harmonic betatron motion requires high energy if $P_z < 0$ (double-well potential), but near-harmonic axis-crossing betatron motion occurs for all $P_z > 0$.

Considering the distribution function of energy and momentum, these linear, axis-crossing betatrons constitute most orbits in the vicinity of the magnetic axis (which Haines refers to as the “singular orbits” on axis³¹). Also common are the nonlinear betatron trajectories (also known as figure-eight motions), which occur for $P_z < 0$ and $H > P_z^2/2m_\alpha$. An important question is: in which direction do these figure-eight motions drift in? Considering Eq. 24 for $\langle \dot{z} \rangle = 0$, one finds

$$\frac{K(\alpha^*)}{E(\alpha^*)} = 2 \implies \alpha^* \approx 0.826. \quad (25)$$

That is, α^* is the critical trapping parameter for which $\langle \dot{z} \rangle = 0$. Thus, betatrons with $0 < \alpha < 0.826$ have drift velocity aligned with the species drift. All motions with $\alpha > 1$ (and $L_\theta = 0$) ∇B drift opposite the species drift, so the range $0.826 < \alpha < \infty$ moves against the species drift velocity. This factor is related to the famous 1.65 correction of the Alfvén current limit²⁸. Of course, the mean velocity of a particle ensemble depends on its distribution function.

Guiding-center theory predicts ∇B drifting ions to drift counter the current, so clearly a naive application of guiding-center theory incorrectly predicts betatron motion. This inapplicability to the betatrons is best understood through the orbit’s adiabatic invariant associated with the radial potential energy, namely the radial action $J_r = m_\alpha \oint v_r^2 dt$. The radial action of the cyclotron orbits is the magnetic moment to $\mathcal{O}(\alpha^{-1})$. In the opposite limit $\alpha \rightarrow 0^+$, the radial action J_r instead represents an adiabatic invariant associated with betatron motion. The radial action of axis-crossing betatron solutions are found in Sonnerup’s 1971 work on the one-dimensional current sheet²⁰.

G. Analytic solution with non-zero angular momentum

The solutions with $L_\theta = 0$ are identical with the one-dimensional current sheet. Exact solutions may also be developed in the cylinder including angular momentum $L_\theta \neq 0$. The method to obtain these solutions is analogous to Y. Hagihara’s celebrated solution of particle motion in the Schwarzschild metric⁴⁸. Hackmann and Lämmerzahl compiled a fairly complete catalogue of analytic solutions on geodesics known up to 2014, including electromagnetic forces⁴⁹. The solution is presented here despite its increased complexity to study the quality of the nonlinear oscillations and their dependence on the three constants of motion H , P_z , and L_θ . The same normalization is adopted as before. To formulate the solution, the singularity at $r = 0$ is removed from the equation of motion by multiplying Eq. 6 by r^2 , yielding

$$\left(\frac{dr^2}{dt}\right)^2 = r^2(e^2 - (P - A)^2) - L^2 \quad (26)$$

where again $e^2 \equiv 2H$ and normalized angular momentum written as L (without subscript). With $A = -r^2/2$ and $\tau \equiv t/\sqrt{2}$, the right-hand-side of Eq. 26 is cubic in A ,

$$\left(\frac{dA}{d\tau}\right)^2 = 4\left(A^3 - 2PA^2 + (P^2 - e^2)A - \left(\frac{L}{2}\right)^2\right). \quad (27)$$

Equation 27 is solved with the theory of elliptic functions. The most general solution is in terms of the Weierstrass elliptic function by changing variables to a depressed cubic. Defining auxiliary

variables $Q \equiv A - 2P/3$ and $N = P/3$ gives

$$\left(\frac{dQ}{d\tau}\right)^2 = 4Q^3 - g_2Q - g_3 \quad (28)$$

where the parameters g_2, g_3 are defined as

$$g_2 = 4(e^2 + 3N^2), \quad (29a)$$

$$g_3 = 8N(e^2 - N^2) + 2L^2. \quad (29b)$$

The general solution of Eq. 28 is Weierstrass's elliptic \wp -function⁵⁰

$$Q = \wp(\tau + \tau_0; g_2, g_3) \quad (30)$$

with τ_0 chosen such that $\wp(\tau_0; g_2, g_3) = Q_0$ at $t = 0$. We are interested in obtaining the period of oscillation associated with Eq. 30. For that reason, we seek the roots (e_1, e_2, e_3) of the polynomial $\mathcal{P}(Q) = 4Q^3 - g_2Q - g_3$, because Eq. 30 can be expressed with Jacobi elliptic functions as

$$\frac{1}{2}r^2(t) = \frac{1}{2}r_0^2 - C\text{sn}^2(\omega t|m) \quad (31)$$

where the elliptic modulus $m \equiv (e_2 - e_3)/(e_1 - e_3)$, the amplitude $C \equiv e_2 - e_3$, and the frequency $\omega \equiv \sqrt{(e_1 - e_3)/2}$. The roots can be found by brute force, for example by Viéte's cubic roots. On the other hand, Eq. 31 combined with $P = \dot{z} + A$ shows that axial velocity satisfies

$$\dot{z}(t) = \dot{z}_0 + C\text{sn}^2(\omega t|m), \quad (32)$$

and therefore one root of the polynomial is $Q^* \equiv N - \dot{z}_0$ such that if the normal form of Eq. 28 were instead written as an equation for \dot{z} , one root would simply be the initial axial velocity \dot{z}_0 , related to the three constants of motion by $(P - \dot{z}_0)(\dot{z}_0^2 - e^2) = L^2/2$, thus reducing the other two roots to a quadratic. After some algebra, a compact form of the roots can be obtained as

$$e_{1,2} = \frac{P}{3} - \dot{z}_0(\alpha \mp \Delta), \quad (33a)$$

$$e_3 = \frac{P}{3} - \dot{z}_0, \quad (33b)$$

$$\Delta \equiv \sqrt{(1 + \alpha)^2 + K_{\parallel 0}/K_{\perp 0}} \quad (33c)$$

where \dot{z}_0 is the initial z -velocity, Δ the quadratic discriminant, and $\alpha \equiv A_0/2\dot{z}_0$ is the trapping parameter (half the ratio of the two momentum components). The discriminant measures the relative importance of the trapping parameter and the initial parallel-to-perpendicular kinetic energy

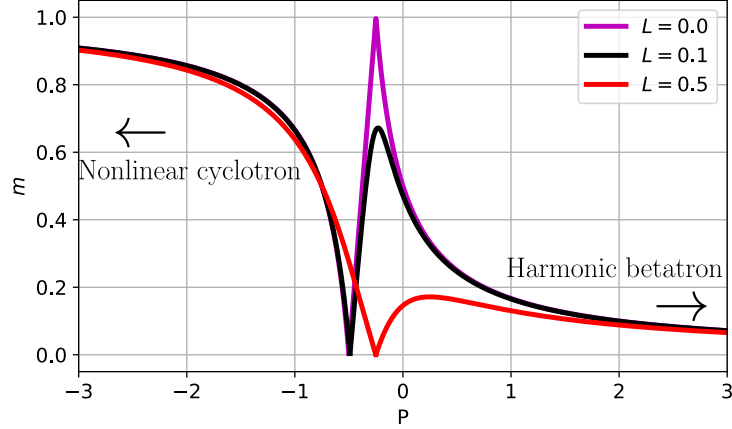


FIG. 5. Variation of the elliptic modulus of Eq. 34 with momentum $P = \dot{z}_0 + A_0$ and angular momentum L for an ion of initial conditions $r_0 = 1$ with $v_{r0} = 0$. When Eq. 34 is negative the modulus is plotted as $\mu = -m/(1-m)$. Oscillations are nonlinear for $m > 0.5$, and otherwise nearly harmonic. The $L = 0$ betatron-cyclotron transition is the sharp peak at $P = -0.25$. There is no clear transition for $L \neq 0$, but the high momentum solution converges to the harmonic betatron oscillation. Momenta $P \ll -1$ execute a nonlinear cycloid motion with period $T \rightarrow 0$ and amplitude $C \rightarrow \infty$ as $P \rightarrow -\infty$.

ratio where $K_{\parallel 0} \equiv (L/r_0)^2/2$ and $K_{\perp 0} \equiv \dot{z}_0^2/2$. When $K_{\parallel 0} = 0$, the roots reduce to $e_{1,3} = N \pm \dot{z}_0$ and $e_2 = N - \dot{z}_0(1 + 2\alpha)$, reducing to the solutions of Section II D. Combination of Eqs. 33a-33c leads to the general elliptic modulus,

$$m = \frac{1 - \alpha - \Delta}{1 - \alpha + \Delta} = m(H, P, L). \quad (34)$$

Equation 34 is an implicit function of H , P , and L , with the compact form involving the parallel and perpendicular energies rather than total energy $H = K_{\perp 0} + K_{\parallel 0}$. When Eq. 34 is negative the solution in Eq. 31 may be evaluated with the transformation in Eq. 16.10.2 of Abramowitz and Stegun⁵¹ to parameter $\mu = -m/(1-m)$. Setting $L = 0$ and choosing $\dot{z}_0 > 0$ recovers the modulus of Section II E. Compared to Eq. 19, Eq. 34 accounts for all values of α and L_{θ} .

The radial oscillation period is $T = 4K(m)$, where negative parameters are treated by⁵¹ $K(-m) = K(m/(1+m))/\sqrt{1+m}$. Considering $\alpha = 0$, a betatron frequency is deduced with $\omega_{\beta}^2 = \sqrt{K_{\perp 0}} + \sqrt{H}$, reducing for $L = 0$ to $\omega_{\beta}^2 = \sqrt{2K_{\perp 0}}$ found before. Cyclotrons inhabit the limit $\alpha \gg 1$, in which to leading-order $m \rightarrow 0$ and $\omega^2 \rightarrow -2A_z$, meaning $\omega^2 \rightarrow \omega_c^2(x)$ in non-normalized units. Thus, the cyclotron-betatron distinction is contained in the trapping parameter despite the nontrivial nature of orbits with angular momentum.

Figure 5 plots the elliptic modulus associated with a particle released from $r_0 = 1$ at zero radial velocity with varying axial and angular velocities. The figure shows that low-energy ions are magnetized linear cyclotrons (with Larmor radius less than the gradient length), high positive-momentum ions are betatrons, and high negative-momentum ions are nonlinear cyclotrons (with Larmor radius much greater than the gradient scale length).

A comment is needed on the just-mentioned nonlinear cyclotron motion, which corresponds to the $\alpha < 0$ regime of Section II D that was not discussed there. The nonlinear cyclotron motion can be understood as a backward-drifting cyclotron motion (that is, essentially cycloidal and not figure-eight or axis-crossing type) with an elliptical orbital period because their Larmor radius exceeds the gradient scale length. Rather than deflecting towards the axis, these orbits are repelled to large radii in a cycloid trajectory. In this sense, they may be considered untrapped motions, as they may exit a finite Z-pinch configuration through contact with solid walls, additional current filaments, etc. Because these orbits execute a cycloidal trajectory we term them nonlinear cyclotrons, as their characteristic frequency is unrelated to the betatron frequency.

1. *Orbit-averaged axial drift with angular momentum*

As in Section II F the orbit-averaged axial drift is computed using Eq. 23 to yield

$$\langle \dot{z} \rangle = \dot{z}_0 \left(1 - (1 - \alpha + \Delta) \left(1 - \frac{E(m)}{K(m)} \right) \right). \quad (35)$$

Equation 35 is a more general formula than Eq. 24, holding for all combinations of parameters provided that when $m < 0$ the elliptic integrals are calculated using the appropriate formulas for negative arguments. The guiding-center velocities are recovered to leading-order in large trapping parameter $\alpha \gg 1$. The various subterms expand as,

$$m = 1 - \alpha^{-1} + \mathcal{O}(\alpha^{-2}), \quad (36a)$$

$$1 - \frac{E(m)}{K(m)} = \frac{1 - \alpha^{-1}}{2} + \mathcal{O}(\alpha^{-2}), \quad (36b)$$

$$1 - \alpha + \Delta = 2 + \frac{K_{\parallel 0}}{2K_{\perp 0}} \alpha^{-1} + \mathcal{O}(\alpha^{-2}), \quad (36c)$$

thus substitution of Eqs. 36a-36c into Eq. 35 gives

$$\langle \dot{z} \rangle = 2 \frac{K_{\parallel 0}}{r_0^2} - \frac{K_{\perp 0}}{r_0^2} + \mathcal{O}(\alpha^{-2}). \quad (37)$$

As $B = r$ (linearly varying field), the first term is the curvature drift $v_{z,c} = 2K_{\parallel}/R_c B_0$ and the second term the grad-B drift $v_{c,\nabla} = -K_{\perp}|\nabla B|/B^2$. As expected from a simple application of the formulas for guiding-center motion, cyclotron particles drift parallel to the current provided that $2K_{\parallel 0} > K_{\perp 0}$ and anti-parallel otherwise.

2. On distinguishing axis-encircling motions

The linear ‘‘helical betatron’’ (Section II C 1, shown in Fig. 2b) has $v_z = \text{const}$ and $v_r = 0$, orbiting in a helix about the electrical current axis with angular velocity equal to the betatron frequency of its orbital radius. Equation 35 shows that $m = 0$ gives $v_z = \text{const}$, from which Eq. 34 gives, solving $(1 + \alpha)^2 + K_{\parallel}/K_{\perp} = (1 - \alpha)^2$,

$$\alpha = \frac{K_{\parallel}}{4K_{\perp}} \quad (38)$$

as the trapping parameter of a helical betatron. Another way of phrasing this is $\frac{K_{\perp}}{K_{\parallel}} = \frac{r}{r_L}$ where r is the axis-encircling orbit radius and $r_L = v_z/\omega_c$ must be understood as the ‘‘characteristic’’ Larmor radius of the helical orbit, and not the radial bounce amplitude which is zero. That is, K_{\perp} accounts only for *axial* kinetic energy, and there is zero *radial* kinetic energy. It is characteristic of betatron motions to exhibit such agyrotropic orbital anisotropy. The helical betatron may be considered a pure curvature drift motion because $v_z = 2K_{\parallel}/R_c B_{\theta}$.

Helical betatrons, having zero radial kinetic energy, inhabit the ground state of the effective potential with $L_{\theta} \neq 0$. Now recall that a small amount of energy on top of the ground state with $L_{\theta} = 0$ characterized the cyclotron orbits with $P_z < 0$. Therefore, it is necessary to clarify when the guiding-center approximation applies to axis-orbiting trajectories. Figure 6 shows examples of such trajectories, with Fig. 6a-c) showing three helical betatron orbits with an additional perturbation of energy out of the ground state. The unperturbed ($K_r = 0$) orbits have trapping parameters of $\alpha = 0.1$, 1.5, and 7.1 respectively for the blue, red, and magenta orbits, as computed by Eq. 38. As suggested by the expansion in Eq. 37, the guiding-center approximation applies to axis-encircling orbits in the limit of large trapping parameters, but not otherwise. Thus, the blue orbit displays non-Larmor betatron motion when some radial energy is added, the red orbit displays a transitional behavior with FLR-corrections to its guiding-center motion, and the magenta trajectory is well-magnetized and governed by the guiding-center theory. In addition, Fig. 6d-f shows how a well-magnetized axis-encircling orbit (in green) is differentiated from a high-energy axis-encircling figure-eight betatron orbit (in orange) in the same effective potential. The axis-encircling figure-eight motion

rotates about the magnetic axis but cannot actually cross it.

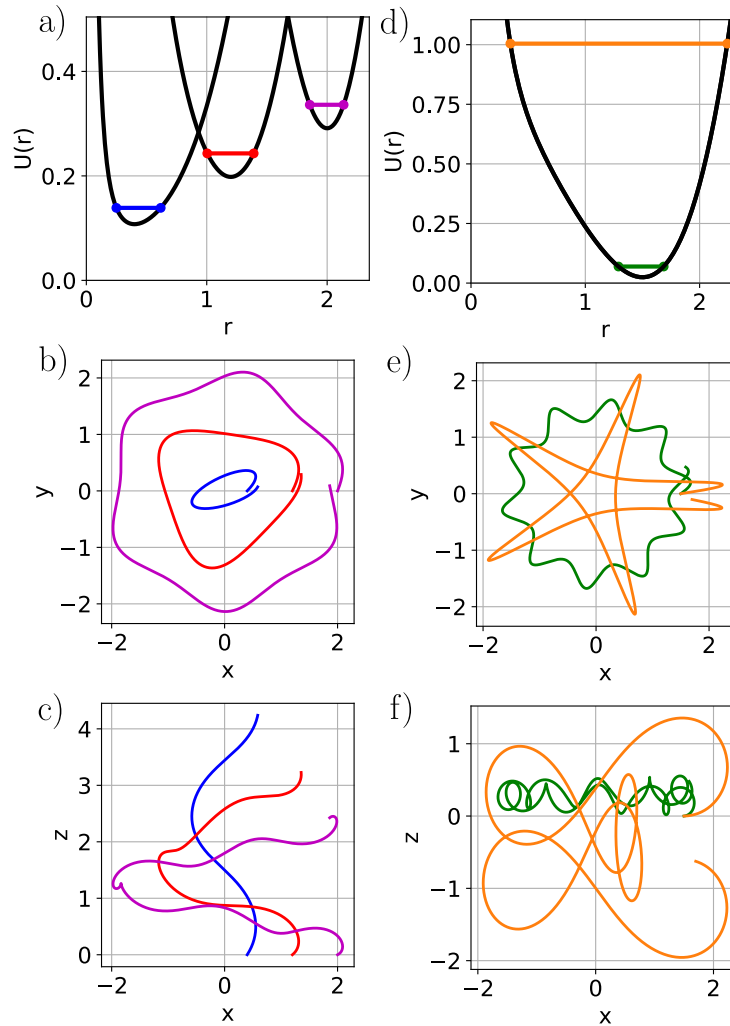


FIG. 6. A study of axis-encircling orbits, with a)-c) displaying the helical betatron-to-cyclotron spectrum in blue, red, and magenta with a small excess energy above the ground state, and parts d)-f) showing a large trapping parameter with non-Larmor betatron motion (orange) in contrast to a well-magnetized orbit (green). The corresponding ground-state helical trajectories of parts a)-c) have trapping parameters of $\alpha = 0.1, 1.5,$ and 7.1 for the blue, red, and magenta orbits respectively. Thus, the excess energy above the ground state results in a well-magnetized cyclotron motion for the magenta orbit, while the red orbit is in the transitional magnetization regime and the blue orbit displays non-Larmor betatron motion. The orange trajectory is noteworthy to show how figure-eight betatron trajectories rotate about the magnetic axis.

3. *Summary of orbital variation with parameters*

To recapitulate the results of Section II, the distinction between cyclotron and betatron motions is contained in the trapping parameter α . For $L_\theta = 0$, the guiding-center approximation works well for cyclotrons whose trapping parameter $\alpha \geq 2$. Cyclotrons are not well-described by guiding-center theory for $1 < \alpha < 2$. The guiding-center theory does not apply to the betatron-type oscillators or the nonlinear cyclotrons, *i.e.* in cases of extreme momentum or energy. All orbits with $P_z > 0$ exhibit radial betatron motion.

The perfectly helical axis-encircling motion is a pure curvature drift. The trapping parameter for such axis-encircling motions ($L_\theta \neq 0$) is related to the ratio of parallel to perpendicular energies. The ∇B -drift is contained in the axis-encircling solutions asymptotically with large trapping parameter. Based on this consideration, axis-encircling motions display radial cyclotron motion only when their trapping parameters $\alpha \gg 1$, thence displaying both curvature drift and ∇B -drift. On the other hand, small trapping parameters display radial betatron motion. Thus, cyclotron and betatron motions are distinguished through the trapping parameter α even for axis-encircling motions. While the betatron frequency characterizes the angular velocity of both cyclotron and betatron axis-encircling motions, the distinction between them is based on the characteristic frequency of their radial motion. Cyclotrons complete a Larmor orbit before completing an orbit about the axis, while betatrons do not.

III. RELATIVE POPULATIONS OF CYCLOTRONS AND BETATRONS

Orbit magnetization governs the transport of particles, momentum, and energy in a plasma. Thus, an important question of practical interest is how the orbits of a given configuration are partitioned between cyclotron and betatron motions. In this section, a criterion is developed to partition the particle phase space into two categories of orbits, and this criterion is applied to the drifting Maxwellian distribution of the Bennett solution²⁹.

A. Trapping condition for cyclotrons

Cyclotron trajectories are differentiated from non-Larmor motions through the trapping parameter. The trapping condition for cyclotrons is expressed in canonical coordinates as

$$\frac{(P_z - q_\alpha A_z)^2}{2m_\alpha} < H < \frac{P_z^2}{2m_\alpha}, \quad (39a)$$

$$-\infty < P_z < \frac{q_\alpha A_z}{2}. \quad (39b)$$

Equations 39 hold exactly for $L_\theta = 0$. The lower limit of H is the minimum possible effective potential energy, and is not a trapping condition but rather the lower limit of the energy domain. The upper limit of H is the trapping condition, being the inner-well height for $P_z < 0$. The upper limit of P_z in Eq. 39b is a trapping parameter cut-off $\alpha > 1$, thereby capturing only cyclotrons.

The trapping condition is modified in a non-trivial manner by orbits with angular momentum, as explored in Section II G. It was found that axis-encircling particles are described by guiding-center theory only if their trapping parameters are large. Combining Eqs. 39 with the trapping parameter (Eq. 19) shows that parallel energies are restricted by the inequality

$$K_r + K_{\parallel} \leq \left(1 - \frac{1}{\alpha}\right) \frac{(q_\alpha A_z)^2}{2m_\alpha}. \quad (40)$$

Therefore, the cyclotron cut-off in Eqs. 39 considers axis-encircling orbits to be well-magnetized only if their trapping parameters are sufficiently greater than unity. For this reason we consider Eqs. 39 to apply also for trajectories with $L_\theta \neq 0$.

The cut-off determined here applies for any axial current profile j_z and associated magnetic vector potential A_z , not just the axis-centered current profiles studied in this work. Considering the sharp pinch for example, trajectories are ballistic within the core (supposing $B = 0$), a transitional magnetization regime occurs in the bounding annular current sheet, and some proportion of trajectories are magnetized within the sheet and outside the sheet. Therefore, the complement to the cyclotron inequalities usually consists of the betatron phase space, but may also describe free-streaming trajectories in flux-free regions. We will now further consider an axis-centered current profile and consider all non-cyclotron orbits to be betatron orbits.

B. Splitting the distribution function into cyclotron and betatron distributions

In this section, we integrate the canonical distribution function of the Bennett pinch over the region of energy-momentum space satisfying the cyclotron cut-off, thereby determining the density

profile of well-magnetized particles. In effect, we split the distribution function into its cyclotron and betatron components and calculate its moments. The result is perspicuously a function only of geometry (characteristic radius) and a magnetization parameter.

As discussed in more detail in the sequel⁹, the Bennett pinch is a kinetic equilibrium, meaning it solves the collisionless kinetic or Vlasov equation²⁹. The distribution function of the Bennett pinch is a drifting Maxwellian with a radial density gradient, which represented in energy/momentum coordinates is

$$f(P_z, H) = Z_\alpha^{-1} \exp(\beta_\alpha u_\alpha P_z) \exp(-\beta_\alpha H) \quad (41)$$

with u_α the species drift, $\beta_\alpha = (k_B T_\alpha)^{-1}$ the inverse temperature, and $Z_\alpha = (\beta_\alpha / 2\pi)^{-3/2} e^{\beta_\alpha m_\alpha u_\alpha^2 / 2}$ is the partition function. The drifting Maxwellian distribution of the Bennett pinch is semi-canonical in the sense that it is exponentially distributed in both energy and momentum, in contrast to the canonical distribution over only energy. Due to the relative motion of electrons and ions sustaining the magnetic field, the Bennett pinch and other magnetic confinement configurations are not in canonical thermodynamic equilibrium despite Maxwellian distributions, in agreement with the Bohr-Van Leeuwen theorem (as noted by E. S. Weibel⁵²).

Axial momentum is exponentially distributed in Eq. 41, which is significant for understanding the distribution of betatron orbits. Positively charged ion trajectories with $P_z > 0$ display radial bounce orbits (and always vice versa for electrons or negatively charged ions), and the distribution function is also exponentially weighted towards $P_z > 0$. Phase space density is weighted towards larger momenta where allowed by the phase space boundary of all particles, as set by $H > H_{\min} = (P_z - q_\alpha A_z)^2 / 2m_\alpha$. Figure 7 shows the phase space in canonical coordinates (P_z, H) depicted for three radii in the transitional magnetization regime. The cyan parabola shows the boundary of Eqs. 39 as the dividing line between cyclotron and betatron populations. Betatrons with $P_z < 0$ display figure-eight orbits rather than radial bounce orbits. The yellow parabola section $(1 - 2\alpha^*)^2 H = P_z^2 / 2m_\alpha$ with $\alpha^* \approx 0.826$ (Eq. 25) shows the dividing line between forward and backward drifting betatron orbits. Note all orbits passing through $r = 0$ are axis-crossing betatron orbits, that the net density is lower at larger radii (because density is peaked on axis), and that progressively more of the population is magnetized at greater radii.

Let us also determine the dividing surface between betatron and cyclotron orbits in velocity space rather than canonical coordinates. The inverse transformation at a given radius is

$$v_r^2 + v_\theta^2 = 2H/m_\alpha - (P_z/m_\alpha - q_\alpha A_z/m_\alpha)^2 \quad (42)$$

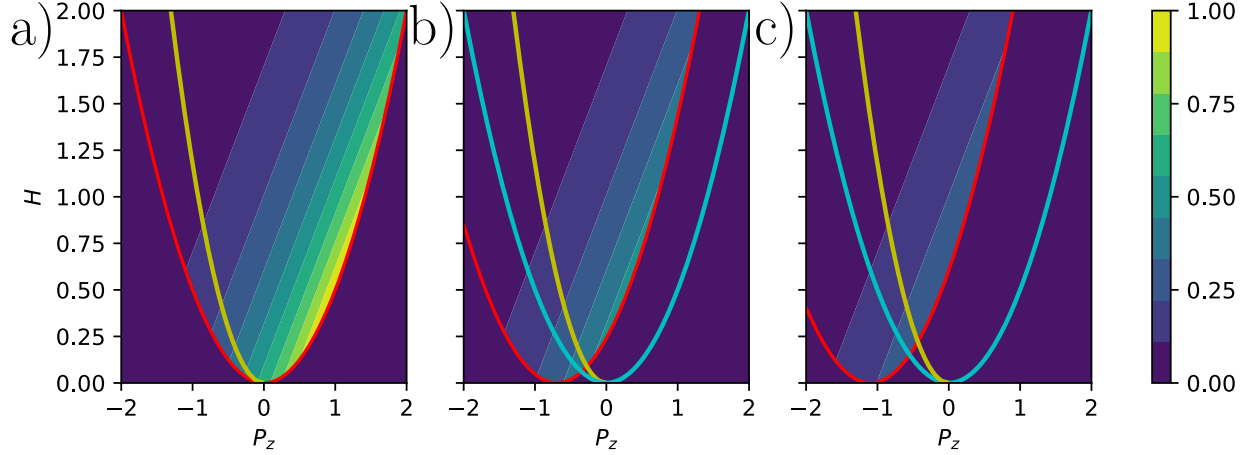


FIG. 7. Phase space density of the Bennett pinch's distribution function (Eq. 41) in the transitional magnetization regime where the Budker parameter $\mathcal{B}_i = 1$ (see Section III D) depicted in canonical energy/momentum coordinates (P_z, H) for a positive charge $q_\alpha > 0$ at radii a) $r = 0$, b) $r = r_p$ and c) $r = \sqrt{2}r_p$. The distribution is normalized to its maximum value at $r = 0$. The red parabola depicts the minimum energy $H_{\min} = (P_z - q_\alpha A_z)^2 / 2m_\alpha$ defining the region of (P_z, H) space occupied by all particles at a particular radius. For positive charges, this defining parabola is shifted towards more negative momenta at larger radii. The left branch of the cyan parabola at $H = P_z^2 / 2m_\alpha$ shows the dividing line between the cyclotron and betatron populations, and the yellow parabola section $(1 - 2\alpha^*)^2 H = P_z^2 / 2m_\alpha$ shows the boundary between forward and backward-drifting betatron orbits. Phase space density to the left of the left branch of the cyan parabola corresponds to well-magnetized cyclotron trajectories, and backward-drifting betatron orbits are contained between the yellow and cyan lines. Betatrons have a positive axial drift velocity to the right of the yellow line. Betatron trajectories with $P_z > 0$ represent radial bounce orbits (what Sonnerup refers to as 'meandering' orbits²⁰), while betatron trajectories with $P_z < 0$ have figure-eight type orbits. All particles passing through $r = 0$ follow betatron trajectories (the red and cyan parabolas coincide). Trajectories associated with the immediate vicinity of the cyan parabola sample the transitional magnetization regime. Progressively more of the population is magnetized at greater radii.

with $m_\alpha v_z = P_z - q_\alpha A_z$. At the dividing energy $H = P_z^2 / 2m_\alpha$, we have

$$1 = \frac{v_r^2}{a_z^2} - 2\frac{v_z}{a_z} + \frac{v_\theta^2}{a_z^2} \quad (43)$$

with $a_z = q_\alpha A_z / m_\alpha$, which represents a paraboloid originating at $v_z = -\frac{1}{2} \frac{q_\alpha A_z}{m_\alpha}$. For $A_z \neq 0$, phase space density of the distribution function enclosed within the paraboloid corresponds to particles

with cyclotron trajectories.

C. Zeroth and first moments of the cyclotron and betatron distributions

Having divided the distribution function into cyclotron and betatron phase space densities, we now calculate their moments. The zeroth moment informs the relative fraction of cyclotron orbits at a particular radius, which is relevant for understanding the validity regime of reduced models reliant on small Larmor radii (such as gyrokinetic theory). The first moment describes the fraction of current carried on average by cyclotron and betatron trajectories, providing a useful means to visualize the balance between the diamagnetic current of cyclotrons and the ‘‘singular current’’ (in the terminology of Haines³¹) or betatron flux.

First, note that integration over velocities is transformed to canonical (P_z, H) coordinates by

$$\begin{aligned} \int_{-\infty}^{\infty} \int_{-\infty}^{\infty} \int_{-\infty}^{\infty} dv_r dv_\theta dv_z f(v_r, v_\theta, v_z) \\ = \int_{-\infty}^{\infty} dP_z \int_{H_{\min}}^{\infty} dH f(P_z, H) \end{aligned} \quad (44)$$

where $H = \frac{m_\alpha}{2}(v_r^2 + v_\theta^2 + v_z^2)$ and $P_z = m_\alpha v_z + q_\alpha A_z$, and energies are restricted by $H > H_{\min} \equiv (P_z - q_\alpha A_z)^2 / 2m_\alpha$. The cyclotron density is found by limiting the bounds in Eq. 44 to the energy-momentum space defined by Eqs. 39 and integrating over the Bennett pinch’s distribution function given by Eq. 41. Thus, the cyclotron density is

$$n_c(A_z) \equiv \int_{-\infty}^{q_\alpha A_z/2} dP_z \int_{H_{\min}}^{P_z^2/2m_\alpha} dH f(P_z, H) \quad (45)$$

and the betatron density is then defined as $n_\beta \equiv n - n_c$. For the Bennett pinch, Eq. 45 simplifies to

$$n_c(r) = \frac{n(r) - n_0}{2} - \frac{n(r)\text{erf}_+ - n_0\text{erf}_-}{2} \quad (46a)$$

$$n_\beta(r) = \frac{n(r) + n_0}{2} + \frac{n(r)\text{erf}_+ - n_0\text{erf}_-}{2} \quad (46b)$$

where $n(r) = n_c + n_\beta$ is the total, unsplit particle density and the functions

$$\text{erf}_\pm \equiv \text{erf}\left(\sqrt{\frac{m_\alpha \beta_\alpha}{2}} \left(u_\alpha \pm \frac{q_\alpha A_z(r)}{2m_\alpha}\right)\right) \quad (47)$$

are error functions evaluated at the drift-shifted vector potential.

The current density carried by the cyclotrons is calculated by the first axial moment,

$$j_c \equiv \frac{q_\alpha}{m_\alpha} \int_{-\infty}^{q_\alpha A_z/2} dP_z (P_z - q_\alpha A_z) \int_{H_{\min}}^{P_z^2/2m_\alpha} dH f(P_z, H), \quad (48)$$

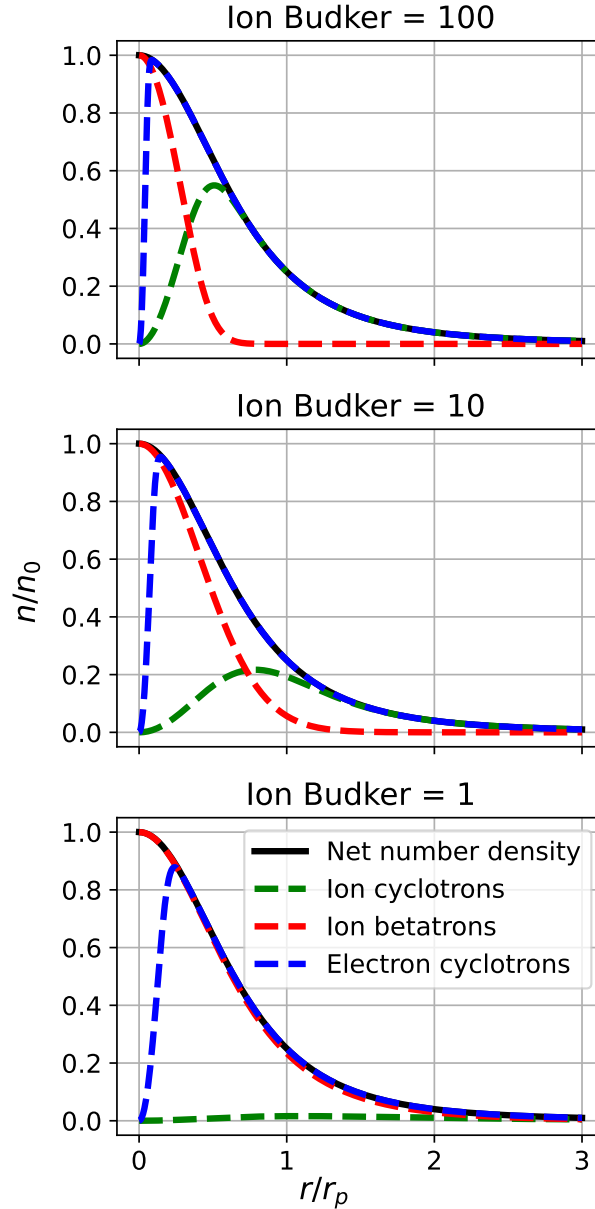


FIG. 8. Partial densities of deuterium ions and electrons in a Bennett pinch equilibrium, split into cyclotrons and betatrons according to Eqs. 46. The ion Budker parameters $\mathfrak{B}_i = (100, 10, 1)$ correspond to particle numbers of $N \approx (10^{20}, 10^{19}, 10^{18}) \text{ m}^{-1}$. The profiles illustrate how the cyclotron-betatron cutoff controls the distribution of orbit magnetization as a function of the species Budker parameter \mathfrak{B}_α , with the species transitional magnetization regime occurring around $\mathfrak{B}_\alpha = 1$. In a certain sense, the ion betatron orbits may be understood to form a beam along the magnetic axis (with radial bounce and axis-encircling spin motions contributing to the radial and azimuthal temperatures of the beam). With $\mathfrak{B}_i = 10$, ion betatron orbits dominate out to the pinch radius $r = r_p$, and by $\mathfrak{B}_i = 1$ nearly all ions display betatron orbits.

so that the partial current densities of cyclotrons and betatrons are given by

$$j_c(r) = \frac{j(r) - j_0}{2} - \frac{j(r)\text{erf}_+ - j_0\text{erf}_-}{2} - j_0\mathfrak{B}_\alpha\text{erfc}_- \quad (49a)$$

$$j_\beta(r) = \frac{j(r) + j_0}{2} + \frac{j(r)\text{erf}_+ - j_0\text{erf}_-}{2} + j_0\mathfrak{B}_\alpha\text{erfc}_+ \quad (49b)$$

where $j(r) = j_c + j_\beta$ is the net current density, \mathfrak{B}_α is the species Budker parameter (given below), and the functions erfc_\pm are as in Eq. 47 but with complementary error functions.

D. Budker parameter: an ensemble-averaged trapping parameter

The argument of the error functions in Eq. 47 (or indeed the parametrization of the Bennett distribution) can be reformulated as a trapping parameter of the particle ensemble (cf. Section II E),

$$\alpha_{\text{ensemble}} \equiv -\frac{1}{2} \frac{q_\alpha A_0}{m_\alpha u_\alpha} = -\frac{q_\alpha A_0}{m_\alpha u_d}, \quad (50)$$

because it is of the same form as the trapping parameter α characterizing individual particle trajectories but is expressed by extensive values. Here A_0 is the characteristic vector potential (e.g., $A_z = A_0 \ln(1 + (r/r_p)^2)$) for the Bennett solution with $A_0 = -\frac{\mu_0}{4\pi} I$, with I total current), u_α is species mean velocity, and $u_d = |u_i - u_e| = 2u_i$ is drift speed.

In 1956, G. I. Budker introduced a parameter to measure the self-field interactions of a charged particle beam of species α as^{53,54}

$$\mathfrak{B}_\alpha \equiv \frac{q_\alpha^2}{4\pi\epsilon_0} \frac{N_\alpha}{m_\alpha c^2} = N_\alpha r_\alpha \quad (51)$$

where N_α is linear density (particles per unit length) and r_α the classical charge radius of species α (when electrostatic self-energy balances mass energy). The extensive trapping parameter (Eq. 50) is precisely the Budker parameter. That is, substitution of the characteristic flux $A_0 = -\frac{\mu_0}{4\pi} I$ and current $I = 2q_\alpha u_\alpha N_\alpha$ (as we have $Z_i = 1$, $N_e = N_i$, and $u_i = -u_e$) into Eq. 50 yields

$$\alpha_{\text{ensemble}} = -\frac{1}{2} \frac{q_\alpha A_0}{m_\alpha u_\alpha} = \frac{\mu_0}{4\pi} \frac{q_\alpha^2 N_\alpha}{m_\alpha} = \frac{q_\alpha^2}{4\pi\epsilon_0} \frac{\epsilon_0 \mu_0 N_\alpha}{m_\alpha} = \mathfrak{B}_\alpha \quad (52)$$

with \mathfrak{B}_α the species Budker parameter. A first identity is immediately established, using the $\beta = 1$ property of the Z-pinch that $\lambda_s = r_{L,s}$, that the Budker parameter admits an interpretation as the

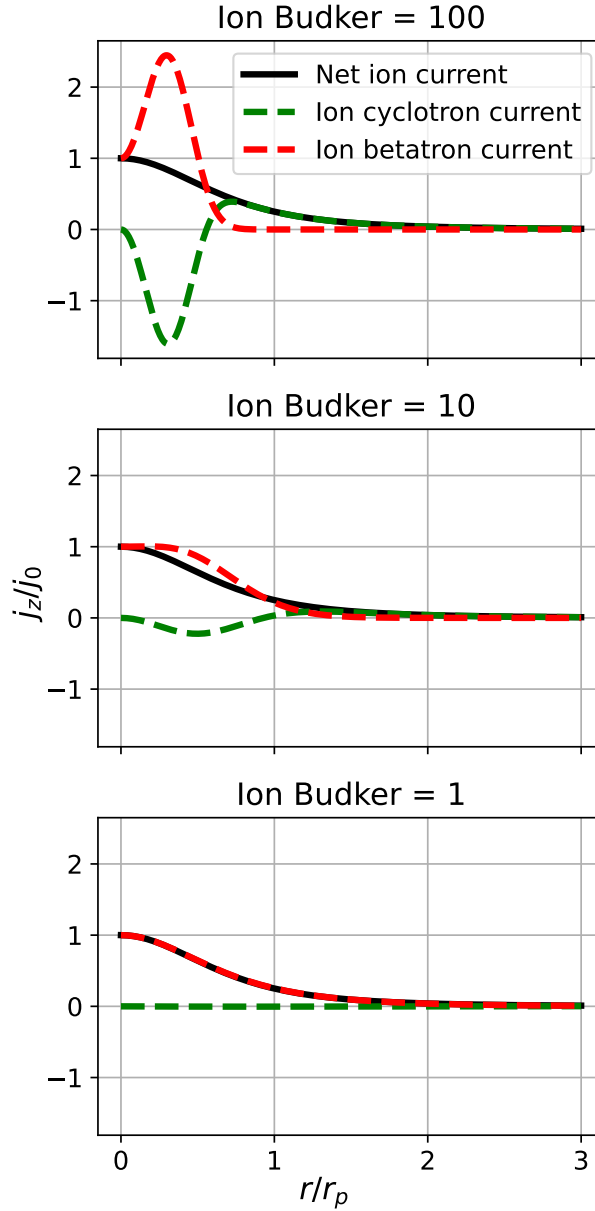


FIG. 9. Partial current densities of deuterium cyclotrons and betatrons in a Bennett pinch equilibrium viewed from the center-of-charge frame according to Eqs. 61 for the Budker parameters of Fig. 8. These current profiles enable a deeper understanding of the interplay between the cyclotrons’ diamagnetic current and the betatrons’ “singular current” (see Haines 1978³¹). Curvature drift is aligned with species drift, but ∇B -drift is anti-aligned. Thus, average guiding-center drift aligns with species drift (carrying species partial current) when curvature drift exceeds ∇B -drift on average. As noted in Section II G, curvature-drifting ions are only cyclotrons if their trapping parameter $\alpha > 1$, and are otherwise betatrons. Therefore, diamagnetic current drifts opposite mean velocity if a majority of curvature-drifting trajectories are betatrons. The resulting backward cyclotron diamagnetic drift is overcome by a net positive betatron velocity in the ion frame.

number of characteristic Larmor radii $r_{L,s}$ or skin depths λ_s within the pinch radius (squared),

$$\mathfrak{B}_\alpha = \frac{\mu_0 q_\alpha^2 N_\alpha}{4\pi m_\alpha} = \frac{\omega_{p\alpha}^2 r_p^2}{4c^2} = \frac{r_p^2}{4\lambda_\alpha^2} = \frac{r_p^2}{4r_{L,\alpha}^2}. \quad (53)$$

A second identity then follows from species thermal crossing time $\tau_\alpha \equiv r_p/v_{t\alpha}$ that

$$\mathfrak{B}_\alpha = \frac{1}{4} \frac{v_{t\alpha}^2}{r_{L,\alpha}^2} \frac{r_p^2}{v_{t\alpha}^2} = \frac{(\omega_{c\alpha} \tau_\alpha)^2}{4} \quad (54)$$

showing an equivalence to the species dynamical Hall parameter. In particular, as a unity- β plasma the ion thermal velocity is related to the characteristic Alfvén speed by $v_{ti}^2 = v_a^2/4$, so the ion Budker parameter is directly equivalent to the ion Alfvén Hall parameter squared, $\mathfrak{B}_i = (\omega_{ci} \tau_a)^2$.

1. Species magnetization fractions

We will now see that the ensemble-averaged trapping parameter, or Budker parameter, characterizes the orbital magnetization regime of an electrical current filament. Regarding the parametrization of the partial densities, observe that substitution of Eq. 52 into Eq. 47 gives

$$\text{erf}_\pm = \text{erf}\left(\frac{1 \pm \mathfrak{B}_\alpha \tilde{A}_z}{\sqrt{2\mathfrak{B}_\alpha}}\right), \quad (55)$$

where $\tilde{A}_z = A_z/A_0$ is normalized magnetic vector potential. Equation 55, together with the cyclotron-betatron splitting (Eqs. 46), shows that the distribution of well-magnetized species in a Bennett equilibrium depends only on the species Budker parameter. As the Budker parameter itself is a function only of the charge carrier inventory (in the sense of linear density), this means that the species magnetization fraction has the same property. This expectation should hold well for center-peaked current profiles (those similar to the Bennett pinch), which available experimental data from the Fusion Z-Pinch Experiment (FuZE) suggests is the case⁵⁵.

Figure 10 shows the fraction of cyclotron particles as a function of Budker parameter in a Bennett equilibrium, determined by numerically integrating Eqs. 46. Considering an ion species, most ions are betatrons in the regime $\mathfrak{B}_i \ll 1$, a transitional occurs around $\mathfrak{B}_i \approx 1$, and most ions are cyclotrons for $\mathfrak{B}_i \gg 1$. To recapitulate, the magnetization regime depends only on the charge carrier inventory (*viz.*, the linear density N). Intuitively, this occurs because, at constant charge flux, axial drift is slower with greater line density. Lower momenta (*viz.* Larmor radii) increase the magnetization of ions in the pinch self-field. The phase space density of Fig. 7 was plotted

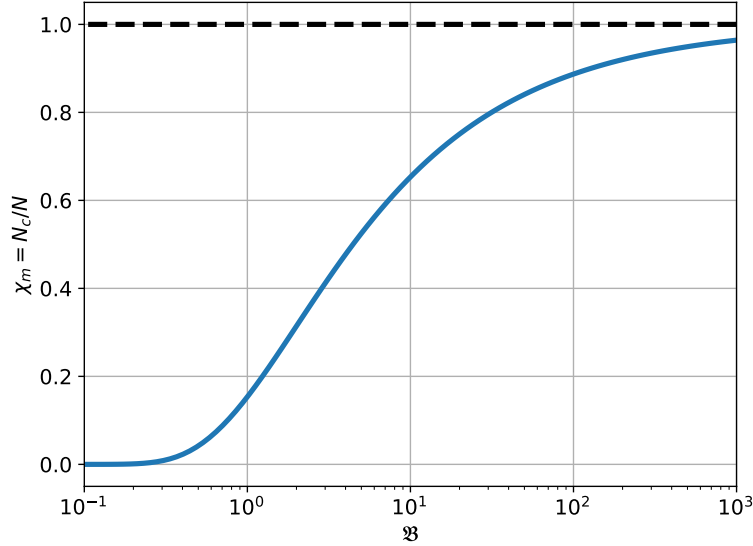


FIG. 10. Magnetization fraction χ_m displayed as a function of Budker parameter \mathfrak{B} . The species subscript is omitted, as the figure applies to both particle species for their respective Budker parameters. Magnetization fraction χ_m is defined as the ratio of linear density of well-magnetized cyclotron particles N_c relative to the total linear particle density composed of both cyclotrons and betatrons $N = N_c + N_\beta$, that is $\chi_m \equiv N_c/N$. The transitional magnetization regime of species α is observed to occur around $\mathfrak{B}_\alpha = 1$.

for $\mathcal{B}_i = 1$. Electrons are mostly cyclotrons for typical experimental linear densities because their lower mass is more easily trapped by the magnetic self-field.

The self-magnetization regime $\mathfrak{B}_\alpha > 1$ occurs when there is more than one drifting particle in a control volume of infinite radial extent and whose axial extent is the classical charge radius. For a deuterium-electron Z-pinch plasma, the critical linear density for electron magnetization is only $N_e^* = r_e^{-1} = 3.5 \times 10^{14} \text{ m}^{-1}$, while deuterium ion magnetization occurs at a greater $N_d^* = r_d^{-1} = 1.3 \times 10^{18} \text{ m}^{-1}$. For typical Z-pinch particle inventories, linear density satisfies $N \gtrsim 1 \times 10^{18} \text{ m}^{-1}$, meaning that electrons are nearly all well-magnetized (besides a “singular” region on-axis) while a significant fraction of ions, particularly within the pinch core, are within the transitional magnetization regime unless $N \gg 1 \times 10^{18} \text{ m}^{-1}$ (see Figs. 8 and 9).

2. Relation to the Alfvén current limit

The Budker parameter is equivalently the current-to-Alfvén limiting current ratio,

$$\mathfrak{B}_\alpha = N_\alpha q_\alpha v_\alpha \frac{q_\alpha}{4\pi\epsilon_0} \frac{1}{m_\alpha v_\alpha c^2} \equiv \frac{I_\alpha}{I_{A,\alpha}} \quad (56)$$

where $I_{A,\alpha} \equiv \frac{4\pi}{\mu_0} \frac{m_\alpha v_\alpha}{q_\alpha}$ is the (species-dependent) Alfvén current limit⁴⁰. The often-cited value of $I_{A,e} = 17\text{kA}$ occurs for electrons at the maximal drift $v_e = c$. Equivalence of the pinch parameter with the Alfvén current is interesting as it clearly connects the theories of neutralized charged particle beams and the Z pinch.

Thus, the Z pinch can be conceptualized as quasineutral, interpenetrating electron and ion beams. From the perfectly neutral Lorentz frame, the difference between an ideal Z pinch and a neutralized charged particle beam is only the relative importance of the self-flux and the drift momentum; ideal beams have $\mathfrak{B}_\alpha \ll 1$, and the ideal Z pinch has $\mathfrak{B}_{e,i} \gg 1$. The interesting transition regime $\mathfrak{B}_\alpha \approx 1$ has both beam/Z-pinch characteristics.

3. The drift parameter and anomalous resistivity

Substitution of the Bennett relation ($\mu_0/8\pi I^2 = 2Nk_B T$, with $T_i = T_e$) into Eq. 51 gives

$$\mathfrak{B}_\alpha^{-1} = \left(\frac{u_\alpha}{v_{t\alpha}} \right)^2. \quad (57)$$

where the species thermal velocity is $v_{t\alpha}^2 = kT_\alpha/m_\alpha$. The drift parameter, or drift Mach number, is often defined as $\chi_d \equiv u_d/v_{ti}$ where $u_d = u_i - u_e$ is the drift speed, and clearly $\chi_d = 2/\sqrt{\mathfrak{B}_i}$. For this reason, one can use the terms ion Budker parameter and drift parameter somewhat interchangeably for a Z pinch, though they are in an inverse-square relation.

It is thought that the anomalous resistivity regime occurs in plasma, both magnetized and unmagnetized, when the drift parameter approaches and exceeds unity⁵⁶. Kinetic instabilities in the pinch will be the subject of a future article, but we summarize here some relevant points. In the case of current perpendicular to the magnetic field in Cartesian slab geometry, the instabilities are known to be of the two-stream kind (including ion-acoustic and Buneman instabilities^{57,58} and the modified two-stream instability⁵⁹) and of the drift wave (or universal) kind^{59,60}.

Equation 57 has the important consequence that the anomalous resistivity regime and ion magnetization are intricately connected. Specifically, the drift parameter $\chi_d = 1$ when most ions are

betatrons and the great majority of electrons are cyclotrons, and this occurs for a particle inventory of $N \approx 10^{18} \text{ m}^{-1}$. This is the basic situation of anomalous resistivity in the Z pinch, although we stress that “unmagnetized” ion orbits are not free-streaming trajectories, but involve radial, axial, and azimuthal charge oscillations at the betatron frequency.

Plasma dynamics which change the linear density of particles also therefore change the orbital magnetization. For example, poor refueling of a flow pinch, and a subsequent dearth of charge carriers, incites a transition simultaneously towards betatron ion orbits and the anomalous resistivity regime. Any process driving pinch radius smaller than the ion skin depth induces anomalous resistivity and thus often current disruptions, such as the recently observed disruption in the Caltech plasma jet experiment⁶¹. There are also many connections to beam generation by $m = 0$ instability such as that explained by Haines³², who showed that ion outflow from the two sides of collapsed hotspots is asymmetric, displaying a preferential flow of high-energy ions to the cathode³.

4. Analogy of self-magnetization to gravitational binding

In terms of the trapping parameter, Eq. 50 $m_\alpha v_\alpha + q_\alpha A_{z,\alpha} = 0$ (with $A_{z,\alpha} = -\frac{\mu_0}{4\pi} I_\alpha$). Therefore, zero ensemble-averaged canonical momentum divides the averaged trapped and untrapped states. Trapped states have negative averaged canonical momentum, while untrapped states have positive averaged canonical momentum. This is analogous to the positive and negative energies of bound and unbound states in the Kepler problem⁶². As shown, the magnetically trapped orbit obeys the laws of guiding-center theory. In some sense the untrapped orbit does as well, but not in a straightforward manner.

Regarding the analogy with static binding, it is interesting to observe that the magnetic force balance is identical to gravitational hydrostatic equilibrium in the cylinder,

$$\frac{1}{r^2} \frac{d}{dr} (r^2 p_g) = -\frac{dp}{dr} \quad (58)$$

where $p_g = g^2/2\mu_g$ is the gravitational pressure with g gravitational acceleration, $\mu_g = 4\pi G$ and G Newton’s constant. The equilibrium equations are identical because the axial vector potential satisfies Poisson’s equation $\nabla^2 A_z = -\mu_0 j_z$ identically to the Newtonian equation $\nabla^2 \Phi_g = -\mu_g \rho$.

In the same procedure as one derives the Bennett relation, Eq. 58 admits a first integral,

$$p' = \frac{\mu_g M'^2}{8\pi} \quad (59)$$

with P' the pressure-energy per unit length and M' the mass per unit length. NB: the classic gravitational binding energy of a spherical mass is $E_g = 3GM^2/5R$ with R the spherical radius, although the virial theorem in the sphere depends on the density profile. Since Eq. 59 is a gravitational binding energy per unit length, the expression of the Bennett relation $P' = \mu_0 I^2 / 8\pi$ may be understood as a magnetic binding energy (per unit length). Comparing the magnetic binding energy (per unit length) to the drift kinetic energy (per unit length) reveals the Budker parameter,

$$\frac{N_\alpha k T_\alpha}{\frac{1}{2} m_\alpha N_\alpha v_\alpha^2} \sim \frac{v_{t,\alpha}^2}{v_\alpha^2} \sim \mathfrak{B}_\alpha. \quad (60)$$

Thus, the Budker parameter admits an interpretation as the ratio of magnetic binding energy to drift kinetic energy, explaining why it coincides with the inverse-square of the drift parameter.

5. *The Hartmann number and viscoresistivity*

The Budker parameter admits yet another interpretation as the Hartmann number Ha , and in this way measures the ratio of magnetoinertial to viscoresistive forces. The Hartmann number itself is the geometric mean of the kinematic Reynolds number R and hydromagnetic Reynolds number (or Lundquist number) S of an Alfvénic flow. The equivalence of the Budker parameter to the Hartmann number has previously been recognized in the Z-pinch literature^{63–66} as the idea that the product of the hydrodynamic Reynolds number and hydromagnetic Lundquist number “is a function only of linear density”. The role of the Hartmann number in regulating plasmas such as the RFP is well-recognized⁶⁷.

To observe the equivalence, suppose that flow is Alfvénic $v = v_a$ (or perhaps that flow shear is Alfvénic, as the velocity at either the core or flux conserver boundary is arbitrary and fixed only through boundary conditions). Next, consider the characteristic length scale to be the pinch radius, $L = r_p$. Under these assumptions, the Reynolds and Lundquist numbers are

$$R = \frac{v_a r_p}{\xi_{\parallel}}, \quad (61a)$$

$$S = \frac{v_a r_p}{\eta_{\parallel}} \quad (61b)$$

where $\xi_{\parallel} = \frac{v_{ti}^2}{\nu_{ii}}$ is the kinematic viscosity due to intraspecies ion diffusion and $\eta_{\parallel} = \lambda_e^2 \nu_{ei}$ (with $\lambda_e = c/\omega_{pe}$) is the magnetic diffusivity in the Spitzer model due to interspecies electron-ion linear friction. In this first approximation we consider the “parallel coefficients” along the axial direction

for a crude model of the betatron effects of axial drift motions. In a large Budker parameter regime the cyclotron orbits must be taken into account, and the scattering rates are in reality likely induced by wave-particle interactions and plasma turbulence.

Considering the viscoresistive product, the inverse relationship in the scattering rates leads to

$$\xi_{\parallel} \eta_{\parallel} = \frac{v_{ei}}{v_{ii}} (c\lambda_D)^2. \quad (62)$$

If the intraspecies ion scattering rate v_{ii} and the interspecies electron scattering rate v_{ei} are in the mass ratio with $v_{ei}/v_{ii} = \sqrt{m_e/m_i}$ then Eq. 62 depends only on the characteristic dissipation scale, namely the Debye length λ_D . In this way, the Debye length directly sets the viscoresistive dissipation level. This property can be broken if the scattering rates are controlled by kinetic processes rather than Coulomb collisions in a manner which does not scale in the mass ratio. Nevertheless, the estimate works quite well in typical laboratory situations. For example, for a hydrogenic plasma, a Debye length of one micron sets the diffusivity scale (as the geometric mean of kinematic and magnetic diffusivities) to $c\lambda_D/(1836)^{1/4} \approx 50 \text{ m}^2/\text{s}$.

Intriguingly, Eq. 62 has units of hyper-diffusivity. Hyper-resistivity and higher-order diffusions are well-known to result from effective viscosity^{68–70}. Typically the effect is due to electron viscosity but ion viscosity, turbulent or neoclassical, can play a similar role due to disparate ion and electron orbit radii and frequency responses^{71,72}.

Now computing the product of the Reynolds and Lundquist numbers of a Z pinch gives

$$RS = \frac{v_a^2 r_p^2}{\xi_{\parallel} \eta_{\parallel}} = \frac{e^2}{4\pi\epsilon_0} \frac{N^2}{\sqrt{m_e m_i} c^2} = \sqrt{\mathfrak{B}_e \mathfrak{B}_i} \quad (63)$$

where the Bennett relation $\mu_0 I^2 / 8\pi = 2NkT$ has been used, together with the Bennett pinch property that half of the total current is enclosed within the pinch radius, $2\pi r_p B_{\theta}(r_p) = \mu_0 I / 2$, and the ions are assumed hydrogenic with $Z_i = 1$ such that $N_e = N_i = N$. Now recognizing that the Hartmann number is defined as

$$\text{Ha} = \frac{v_a L}{\sqrt{\xi_{\parallel} \eta_{\parallel}}} \quad (64)$$

we obtain that $\text{Ha}^2 = \sqrt{\mathfrak{B}_e \mathfrak{B}_i}$. Thus, the Hartmann number squared of a flow pinch is the geometric mean of the electron and ion Budker parameters. If we measure using the ion Budker parameter with $\mathfrak{B}_e = \frac{m_i}{m_e} \mathfrak{B}_i$, then $\text{Ha} \approx 7.8 \sqrt{\mathfrak{B}_i}$ for an electron-deuterium plasma. The numerical factor will be modified by induced scattering effects.

E. Interplay of diamagnetic cyclotron current and betatron current

Magnetization fraction plays a key role in the dynamics of the diamagnetic current in the Z pinch. Figure 9 shows the radial profiles of current carried by cyclotron and betatron ions (as viewed from the center-of-charge frame) as a function of radius. Electrons are well-magnetized for most particle inventories of experimental interest, so our commentary focuses on the ion current contribution. In the regime $\mathfrak{B}_i \gg 1$ most ions are magnetized. However, Fig. 9 displays an important feature for $\mathfrak{B}_i \gg 1$, namely a backward flow of cyclotrons canceled out by a forward flow of betatrons³¹. This indicates the equilibrium between the cyclotrons’ diamagnetic current and the betatrons’ “singular current”.

For guiding-center particles, curvature drift is aligned with the species mean drift velocity, but ∇B -drift is anti-aligned. Thus, guiding-center drifts only align with species drift (thus “carrying” species partial current) if ensemble-averaged curvature drift exceeds ∇B -drift. As noted in Section II G, curvature-drifting ions are cyclotrons only if their trapping parameter $\alpha > 1$ and otherwise are betatrons. Therefore, the diamagnetic current is *opposite* mean species velocity if most curvature-drifting trajectories are betatrons, because most cyclotrons are undergo the backward-oriented ∇B -drift. The ion betatrons have net positive velocity (in the ion frame) to overcome the backward ion cyclotron drift.

On the other hand, curvature drift enables diamagnetic current conduction when most axis-encircling particles satisfy the trapping condition $\alpha > 1$. Thus, current is conducted entirely by cyclotrons at sufficiently large radii. Figure 9 shows that for modest particle inventories $N \approx 10^{19} - 10^{20} m^{-1}$, the transition between betatron and diamagnetic ion current conduction occurs in the vicinity of the pinch radius.

It is illustrative to summarize the example considered by Haines³¹ of a hot, static ion population in the laboratory frame wherein the mean electron velocity sustains the laboratory-frame current $\mathbf{j} = -nev_e$. When the ion distribution is divided into cyclotron and betatron parts, counter-streaming fluxes of cyclotrons and betatrons are observed in the vicinity of the axis, consisting of anode-to-cathode directed ion betatron flux through a counter-streaming ion cyclotron flux. The positive ion betatron flux is balanced to net zero ion flux by the negatively directed diamagnetic ion cyclotron current.

Therefore, there exists a flux of betatron ions from anode to cathode even with zero ion fluid velocity. The same effect occurs for electrons in a thin (“singular” in Haines’ terminology⁷³) layer

around the axis. Beyond this singular layer, curvature drifting electron cyclotrons conduct all electron current. To make generalized statements applicable to modest parameter regimes, these considerations suggest that Z-pinch current is carried by cyclotron electrons and betatron ions which balance and overcome diamagnetic fluxes.

We now extend Haines' thought process to the flow pinch. In FuZE¹, the plasma flow is directed from cathode to anode with $\mathbf{j} \cdot \mathbf{v} < 0$ (opposite the current), meaning that the ion fluid velocity is directed opposite the expected ion betatron drift. In the laboratory frame, the significance is (for moderate parameters, say $\mathfrak{B}_i = \mathcal{O}(10)$) that ion betatrons radially oscillate with reduced or even zero axial drift via the motional radial electric field. Cathode-to-anode-directed ion fluid velocity on the order of the drift velocity thereby reduces the betatron ion current effect of Haines 1978³¹.

1. Possibility of kinetic instabilities driven by relative cyclotron-betatron drift

Here we consider the question of the kinetic stability of a Z pinch in light of the cyclotron and betatron distributions, and a thorough study of kinetic stability is left for future work. Given that the two trajectories display distinct characteristic frequencies (especially for $\mathfrak{B} \gg 1$), it appears that the separated cyclotron and betatron distributions will contribute to distinct collective motions hybridized with the plasma oscillations. For instance, collective betatron modes are known to arise in the dispersion analysis of electron beams^{74,75}. Thus, the oscillation spectrum of the Bennett pinch should depend on the Budker parameter.

Considered as distinct distributions with their own mean velocities, it is plausible that the cyclotron-plasma and betatron-plasma oscillations may themselves couple. Given the high relative velocity between cyclotron and betatron populations within the “diamagnetic layer” described in Section III E, these coupled oscillations may drive kinetic instabilities. It is possible that these kinetic instabilities may drive towards a sharp pinch profile, with an enhanced fraction of betatron particles that carry the current in the Z-pinch core.

IV. THE ROLE OF THE RADIAL ELECTRIC FIELD

Section II A observed that the radial electric field associated with sheared axial flow can influence the detailed motion of charges. In this section, we consider the model shear flow (Eq. 2) in which the flow velocity in the center-of-charge frame is $v_z = \gamma q_i \psi'_\theta / m_i$ where ψ'_θ is the magnetic flux

per unit length. When the constant $\gamma < 0$ the electric field points radially outward, and the fluid vorticity $\boldsymbol{\omega} = \nabla \times \boldsymbol{v}$ aligns counter the magnetic field such that $\boldsymbol{B} \cdot \boldsymbol{\omega} < 0$, the orientation known to be stabilizing for $m = 0$ modes^{76–78}.

Consider the effective potential for particles orbiting in the (r, z) -plane with $L_\theta = 0$,

$$U = \frac{(P_z - q_i A_z)^2}{2m_i} + \gamma \frac{(q_i A_z)^2}{2m_i}. \quad (65)$$

Figure 11 plots the effective potential and shows that the stabilizing shear orientation increases the range of energies associated with cyclotron motion. This is most evident for small values of P_z ,

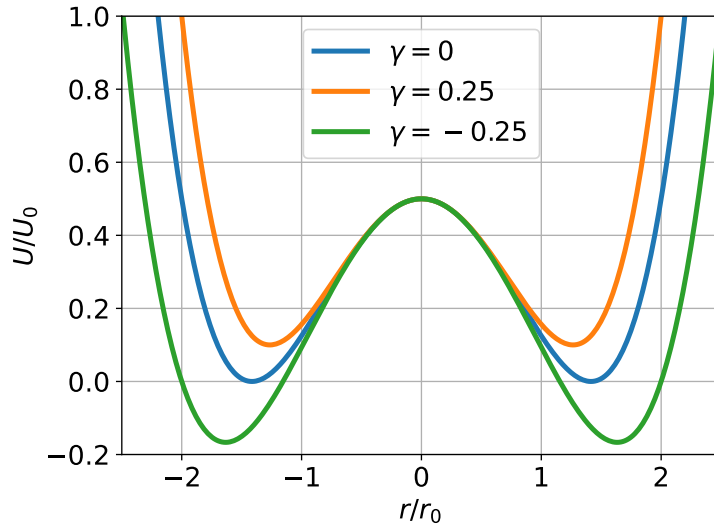


FIG. 11. The effective potential (Eq. 65) including the radial electric field potential arising from a model shear flow (Eq. 2), plotted in normalized units wherein $A_z = -r^2/2$ and $P_z = -1$. The energy level of the separatrix dividing cyclotron and betatron motion is unchanged by the radial field (at the energy for which $E = U(r = 0)$), but the range of energy corresponding to cyclotrons is changed by the depth of the well.

hence, the nature of an orbit is most influenced by the radial electric field within the pinch radius. The conditions for cyclotron trapping of a particle (*i.e.* that its energy and momentum levels leave it confined within the inner well of Fig. 11) are accordingly changed from Eqs. 39 into

$$\frac{(P_z - qA_z)^2}{2m_i} + \gamma \frac{(qA_z)^2}{2m_i} < H < \frac{P_z^2}{2m_i}, \quad (66a)$$

$$-\infty < P_z < (1 + \gamma) \frac{q_i A_z}{2}. \quad (66b)$$

Carrying out the procedure of Section III to estimate the cyclotron and betatron densities, we obtain

an identical solution to Eqs. 46 with a different argument to the error functions,

$$\text{erf}_{\pm} = \text{erf}\left(\frac{1 \pm (1 \mp \gamma)\mathfrak{B}_i \tilde{A}_z}{\sqrt{2\mathfrak{B}_i}}\right). \quad (67)$$

Equation 67 reveals that the radial electric field associated with sheared flow influences macroscopic ion magnetization, modifying the magnetization parameter by an amount $(1 + \gamma)^2$, as the factor in front of \tilde{A}_z controls the location and thickness of the transitional magnetization layer. The radial electric field correction to ion magnetization is most important for the marginal boundary of the transitional magnetization regime around $\mathfrak{B}_i \approx 1$, which is also the anticipated anomalous resistivity regime⁵⁷. Thus, radial electric field influence on ion magnetization is expected to be an important consideration for kinetic physics in the Z pinch.

In closing, we note that the effective potential of Eq. 65 is solvable in elliptic functions with arbitrary angular momentum, as in Section II G. The leading cubic coefficient of the differential equation is modified to $(1 + \gamma)A^3$ in Eq. 27, which can significantly alter the nature of the solution. However, we do not pursue the analytic solution here.

V. GENERAL DISCUSSION

Particle drifts are a central consideration for transport and compressibility in plasmas. To elucidate such drifts, variable trajectory magnetization in the pinch was studied beginning with analytic solutions in a uniform current density. The analytic solutions contain two essential varieties of drifts characterized respectively by cyclotron and betatron frequencies.

The modulus of the analytic solution connecting cyclotron and betatron motion is quantified by two parameters, a magnetic trapping parameter and the ratio of field-parallel to field-perpendicular kinetic energies. This modulus determines the energy and momentum phase-space boundary between characteristic cyclotron and betatron trajectories in a given field. This insight was applied to determine the orbital structure of the canonical equilibrium distribution (the Bennett solution), which was averaged over to obtain the number and current densities of the cyclotron and betatron trajectories. These densities depend only on an ensemble-averaged trapping parameter for that plasma species.

This ensemble-averaged trapping parameter is precisely the Budker parameter \mathfrak{B}_s , which measures the self-magnetic interaction of charged particle beams. The Budker parameter depends only on fundamental single-particle constants such as mass and charge and the linear number density N_s ,

which can be understood as the charge carrier inventory. The ion and electron Budker parameters are related in the mass ratio $\mathfrak{B}_e = \frac{m_i}{m_e} \mathfrak{B}_i$, meaning that electrons are well-magnetized even in the transitional ion regime $\mathfrak{B}_i \approx 1$.

In general, the diffuse pinch is composed of cyclotron orbits in the magnetized periphery, betatron orbits in the current-dense core, and in-between of a transitional magnetization layer whose location and thickness is parametrized by \mathfrak{B}_s . A caveat is that the magnetization regimes are not strictly spatially dependent since magnetization depends on both energy and canonical momentum. In other words, the phase space boundary between cyclotron and betatron distributions is energy- and momentum-dependent, forming a parabola in canonical coordinates or a paraboloid in the velocity space, and the partial number and current densities are reduced descriptions of phase space distributions. The sequel to this work⁹ uses these results to study the influence of ion orbit magnetization on collisionless adiabatic compression and viscosity of the pinch.

The Budker parameter characterizing particle magnetization is equivalent to a multitude of alternative parameters, one of which is the drift parameter u_d/v_{ti} characterizing streaming and drift-type kinetic instabilities. The resulting plasma fluctuations produce anomalous resistivity, thereby limiting practical ion Budker parameters $\mathfrak{B}_i > 1$ and otherwise greatly increasing the power-coupling requirement. Ion orbit magnetization also governs viscosity in the flow pinch, which is associated with thermal anisotropies. In the sequel, anisotropy of an Alfvénic shear flow is found to scale with the drift parameter as well, indicating the potential for anisotropy-induced kinetic instabilities to play a key role in viscosity in the regime $\mathfrak{B}_i = \mathcal{O}(1)$.

ACKNOWLEDGMENTS

The authors would like to thank A.D. Stepanov for bringing to our attention the understanding in the beams community that the Budker parameter quantifies self-field interactions. The information, data, or work presented herein is based in part upon work supported by the National Science Foundation under Grant No. PHY-2108419.

AUTHOR DECLARATIONS

Conflict of Interest

The authors have no conflicts to disclose.

Author Contributions

Daniel W. Crews: Conceptualization (lead), Formal analysis (lead), Investigation (lead), Methodology (lead), Writing - original draft (lead), Writing - review and editing (lead). **Eric T. Meier:** Conceptualization (equal), Project Administration (equal), Supervision (equal), Writing - review & editing (equal). **Uri Shumlak:** Conceptualization (equal), Project Administration (equal), Supervision (equal), Writing - review & editing (equal).

Data Availability

The data that support the findings of this study are available from the corresponding author upon reasonable request.

REFERENCES

- ¹U. Shumlak, “Z-pinch fusion,” *Journal of Applied Physics* **127**, 200901 (2020), https://pubs.aip.org/aip/jap/article-pdf/doi/10.1063/5.0004228/19782092/200901_1_online.pdf.
- ²B. B. Kadomtsev, “Hydromagnetic stability of a plasma,” *Reviews of Plasma Physics* **2**, 153–199 (1966).
- ³V. V. Vikhrev and V. D. Korolev, “Neutron generation from Z-pinch,” *Plasma Physics Reports* **33**, 356–380 (2007).
- ⁴U. Shumlak, R. P. Golingo, B. A. Nelson, and D. J. Den Hartog, “Evidence of stabilization in the Z-pinch,” *Phys. Rev. Lett.* **87**, 205005 (2001).
- ⁵B. Levitt, C. Goyon, J. T. Banasek, S. C. Bott-Suzuki, C. Liekhus-Schmaltz, E. T. Meier, L. A. Morton, A. Taylor, W. C. Young, B. A. Nelson, D. A. Sutherland, M. Quinley, A. D. Stepanov, J. R. Barhydt, P. Tsai, K. D. Morgan, N. van Rossum, A. C. Hossack, T. R. Weber, W. A. McGehee, P. Nguyen, A. Shah, S. Kiddy, M. Van Patten, A. E. Youmans, D. P. Higginson, H. S. McLean, G. A. Wurden, and U. Shumlak, “Elevated Electron Temperature Coincident with Observed Fusion Reactions in a Sheared-Flow-Stabilized Z Pinch,” *Phys. Rev. Lett.* **132**, 155101 (2024).
- ⁶Y. Zhang, U. Shumlak, B. A. Nelson, R. P. Golingo, T. R. Weber, A. D. Stepanov, E. L. Claveau, E. G. Forbes, Z. T. Draper, J. M. Mitrani, H. S. McLean, K. K. Tummel, D. P. Higginson, and C. M. Cooper, “Sustained neutron production from a sheared-flow stabilized z pinch,” *Phys. Rev. Lett.* **122**, 135001 (2019).

- ⁷J. M. Mitrani, J. A. Brown, B. L. Goldblum, T. A. Laplace, E. L. Claveau, Z. T. Draper, E. G. Forbes, R. P. Golingo, H. S. McLean, B. A. Nelson, U. Shumlak, A. Stepanov, T. R. Weber, Y. Zhang, and D. P. Higginson, “Thermonuclear neutron emission from a sheared-flow stabilized Z-pinch,” *Physics of Plasmas* **28**, 112509 (2021), https://pubs.aip.org/aip/pop/article-pdf/doi/10.1063/5.0066257/13408570/112509_1_online.pdf.
- ⁸I. Datta, E. Meier, and U. Shumlak, “Whole device modeling of the fuze sheared-flow-stabilized z pinch,” *Nuclear Fusion* **64**, 066016 (2024).
- ⁹D. W. Crews, E. T. Meier, and U. Shumlak, “Z Pinch Kinetics II - A Continuum Perspective: Betatron Heating and Self-Generation of Sheared Flows,” In preparation (2024).
- ¹⁰T. G. Northrop, “The guiding center approximation to charged particle motion,” *Annals of Physics* **15**, 79–101 (1961).
- ¹¹H. Che, C. Schiff, G. Le, J. C. Dorelli, B. L. Giles, and T. E. Moore, “Quantifying the effect of non-Larmor motion of electrons on the pressure tensor,” *Physics of Plasmas* **25**, 032101 (2018), https://pubs.aip.org/aip/pop/article-pdf/doi/10.1063/1.5016853/16152069/032101_1_online.pdf.
- ¹²B. H. Ripin, E. A. McLean, C. K. Manka, C. Pawley, J. A. Stamper, T. A. Peyser, A. N. Mostovych, J. Grun, A. B. Hassam, and J. Huba, “Large-Larmor-radius interchange instability,” *Phys. Rev. Lett.* **59**, 2299–2302 (1987).
- ¹³D. E. George and J.-M. Jahn, “Energized oxygen in the magnetotail: Current sheet bifurcation from speiser motion,” *Journal of Geophysical Research: Space Physics* **125**, e2019JA027339 (2020), e2019JA027339 10.1029/2019JA027339, <https://agupubs.onlinelibrary.wiley.com/doi/pdf/10.1029/2019JA027339>.
- ¹⁴H. O. Åkerstedt, “Gyrokinetic stability theory of Z-pinch,” *Journal of Plasma Physics* **44**, 137–149 (1990).
- ¹⁵R. C. Davidson and H. Qin, *Physics of Intense Charged Particle Beams in High Energy Accelerators* (CO-PUBLISHED WITH WORLD SCIENTIFIC PUBLISHING CO, 2001) <https://www.worldscientific.com/doi/pdf/10.1142/p250>.
- ¹⁶H. Alfvén, “Some properties of magnetospheric neutral surfaces,” *Journal of Geophysical Research (1896-1977)* **73**, 4379–4381 (1968), <https://agupubs.onlinelibrary.wiley.com/doi/pdf/10.1029/JA073i013p04379>.
- ¹⁷E. N. Parker, “Newtonian Development of the Dynamical Properties of Ionized Gases of Low Density,” *Phys. Rev.* **107**, 924–933 (1957).

- ¹⁸T. W. Speiser, “Particle trajectories in model current sheets: 1. Analytical solutions,” *Journal of Geophysical Research (1896-1977)* **70**, 4219–4226 (1965), <https://agupubs.onlinelibrary.wiley.com/doi/pdf/10.1029/JZ070i017p04219>.
- ¹⁹T. W. Speiser, “Particle trajectories in model current sheets: 2. Applications to auroras using a geomagnetic tail model,” *Journal of Geophysical Research (1896-1977)* **72**, 3919–3932 (1967), <https://agupubs.onlinelibrary.wiley.com/doi/pdf/10.1029/JZ072i015p03919>.
- ²⁰B. U. Ö. Sonnerup, “Adiabatic particle orbits in a magnetic null sheet,” *Journal of Geophysical Research (1896-1977)* **76**, 8211–8222 (1971), <https://agupubs.onlinelibrary.wiley.com/doi/pdf/10.1029/JA076i034p08211>.
- ²¹J. Büchner and L. M. Zelenyi, “Regular and chaotic charged particle motion in magnetotail-like field reversals: 1. basic theory of trapped motion,” *Journal of Geophysical Research: Space Physics* **94**, 11821–11842 (1989), <https://agupubs.onlinelibrary.wiley.com/doi/pdf/10.1029/JA094iA09p11821>.
- ²²M. Hesse, K. Schindler, J. Birn, and M. Kuznetsova, “The diffusion region in collisionless magnetic reconnection,” *Physics of Plasmas* **6**, 1781–1795 (1999), https://pubs.aip.org/aip/pop/article-pdf/6/5/1781/19073083/1781_1_online.pdf.
- ²³J. T. Dahlin, J. F. Drake, and M. Swisdak, “The mechanisms of electron heating and acceleration during magnetic reconnection,” *Physics of Plasmas* **21**, 092304 (2014), https://pubs.aip.org/aip/pop/article-pdf/doi/10.1063/1.4894484/13778511/092304_1_online.pdf.
- ²⁴E. P. Alves, J. Zrake, and F. Fiuza, “Nonthermal ion acceleration by the kink instability in nonrelativistic jets,” *Physics of Plasmas* **26**, 072105 (2019), https://pubs.aip.org/aip/pop/article-pdf/doi/10.1063/1.5098478/19753591/072105_1_online.pdf.
- ²⁵M. Lemoine, “Particle transport through localized interactions with sharp magnetic field bends in MHD turbulence,” *Journal of Plasma Physics* **89**, 175890501 (2023).
- ²⁶J. M. TenBarge, J. Juno, and G. G. Howes, “Electron energization in reconnection: Eulerian vs Lagrangian perspectives,” *Physics of Plasmas* **31**, 022901 (2024), https://pubs.aip.org/aip/pop/article-pdf/doi/10.1063/5.0184710/19725186/022901_1_5.0184710.pdf.
- ²⁷A. J. Brizard, “On the validity of the guiding-center approximation in the presence of strong magnetic gradients,” *Physics of Plasmas* **24**, 042115 (2017), https://pubs.aip.org/aip/pop/article-pdf/doi/10.1063/1.4981217/15625468/042115_1_online.pdf.
- ²⁸H. Alfvén, “On the motion of cosmic rays in interstellar space,” *Phys. Rev.* **55**, 425–429 (1939).

- ²⁹W. H. Bennett, “Magnetically self-focussing streams,” *Phys. Rev.* **45**, 890–897 (1934).
- ³⁰O. Buneman, “The Bennett Pinch,” *Plasma Physics* **60**, 202 (1961).
- ³¹M. G. Haines, “Particle orbits, diamagnetism, and energy balance in a Z-pinch satisfying the Lawson criterion,” *Journal of Physics D: Applied Physics* **11**, 1709 (1978).
- ³²M. G. Haines, “Ion beam formation in an $m = 0$ unstable Z pinch,” *Nuclear Instruments and Methods in Physics Research* **207**, 179–185 (1983).
- ³³M. G. Haines, “Kinetic effects in Z pinches,” *Laser and Particle Beams* **19**, 345–353 (2001).
- ³⁴M. G. Haines, “A review of the dense Z-pinch,” *Plasma Physics and Controlled Fusion* **53**, 093001 (2011).
- ³⁵E. V. Belova, R. C. Davidson, H. Ji, and M. Yamada, “Kinetic effects on the stability properties of field-reversed configurations. I. Linear stability,” *Physics of Plasmas* **10**, 2361–2371 (2003), https://pubs.aip.org/aip/pop/article-pdf/10/6/2361/19211232/2361_1_online.pdf.
- ³⁶P. Gratreau, “Generalized Bennett equilibria and particle orbit analysis of plasma columns carrying ultra-high currents,” *The Physics of Fluids* **21**, 1302–1311 (1978), https://pubs.aip.org/aip/pfl/article-pdf/21/8/1302/12259969/1302_1_online.pdf.
- ³⁷D. J. Griffiths, “Resource Letter EM-1: Electromagnetic Momentum,” *American Journal of Physics* **80**, 7–18 (2012), https://pubs.aip.org/aapt/ajp/article-pdf/80/1/7/13118704/7_1_online.pdf.
- ³⁸L. D. Landau and E. M. Lifshitz, *Quantum mechanics: non-relativistic theory*, Vol. 3 (Elsevier, 2013).
- ³⁹R. C. Davidson and C. Chen, “Kinetic description of high intensity beam propagation through a periodic focusing field based on the nonlinear Vlasov-Maxwell equations,” *Part. Accel.* **59**, 175–250 (1998).
- ⁴⁰I. Y. Dodin and N. J. Fisch, “Correction to the Alfvén-Lawson criterion for relativistic electron beams,” *Physics of Plasmas* **13**, 103104 (2006), https://pubs.aip.org/aip/pop/article-pdf/doi/10.1063/1.2358970/15623465/103104_1_online.pdf.
- ⁴¹D. W. Crews and U. Shumlak, “Phase space eigenfunctions with applications to continuum kinetic simulations,” (2024), [arXiv:2402.02180 \[physics.plasm-ph\]](https://arxiv.org/abs/2402.02180).
- ⁴²In a magnetic well sustained by $+z$ -directed electric current $j_z > 0$, the magnetic potential decreases away from the axis and can be chosen to be always negative.
- ⁴³S. Weinberg, “General Theory of Resistive Beam Instabilities,” *Journal of Mathematical Physics* **8**, 614–641 (1967), https://pubs.aip.org/aip/jmp/article-pdf/8/3/614/19327833/614_1_online.pdf.

- ⁴⁴U. Krishnamurthi, A. S. Sharma, and A. Sen, “Kinetic theory of the $m = 1$ kink instability in Z-pinches,” *Nuclear Fusion* **28**, 789 (1988).
- ⁴⁵A. J. Brizard, “A primer on elliptic functions with applications in classical mechanics,” *European Journal of Physics* **30**, 729 (2009).
- ⁴⁶W. P. Reinhardt and P. L. Walker, “Jacobian Elliptic Functions,” in *NIST Handbook of Mathematical Functions* (Cambridge University Press, 2010) Chap. 22.
- ⁴⁷In Brizard 2017, the guiding-center displacement can be put into the form $\frac{r_L}{4\alpha}$, which differs from our $\frac{5r_L}{4\alpha}$ by a Larmor radius. The difference is that the displacement in Brizard 2017 is measured from the guiding-center of the cycloid while here, for convenience, the displacement is measured from the edge of the cycloid, accounting for the extra factor.
- ⁴⁸Y. Hagihara, “Theory of the Relativistic Trajectories in a Gravitational Field of Schwarzschild,” *Japanese Journal of Astronomy and Geophysics* **8**, 67 (1930).
- ⁴⁹E. Hackmann and C. Lämmerzahl, “Analytical solution methods for geodesic motion,” *AIP Conference Proceedings* **1577**, 78–88 (2014), https://pubs.aip.org/aip/acp/article-pdf/1577/1/78/11408794/78_1_online.pdf.
- ⁵⁰G. Pastras, “Four Lectures on Weierstrass Elliptic Function and Applications in Classical and Quantum Mechanics,” (2017), [arXiv:1706.07371 \[math-ph\]](https://arxiv.org/abs/1706.07371).
- ⁵¹M. Abramowitz and I. A. Stegun, *Handbook of mathematical functions with formulas, graphs, and mathematical tables*, Vol. 55 (US Government printing office, 1968).
- ⁵²E. S. Weibel, “On the Confinement of a Plasma by Magnetostatic Fields,” *The Physics of Fluids* **2**, 52–56 (1959), https://pubs.aip.org/aip/pfl/article-pdf/2/1/52/12438964/52_1_online.pdf.
- ⁵³G. I. Budker, “Relativistic stabilized electron beam,” *The Soviet Journal of Atomic Energy* **1**, 673–686 (1956).
- ⁵⁴R. C. Davidson, *Physics of nonneutral plasmas* (World Scientific Publishing Company, 2001).
- ⁵⁵C. Goyon, S. C. Bott-Suzuki, A. E. Youmans, J. T. Banasek, L. A. Morton, B. Levitt, J. R. Barhydt, K. D. Morgan, C. Liekhus-Schmaltz, W. C. Young, D. P. Higginson, A. C. Hossack, E. T. Meier, B. A. Nelson, M. Quinley, A. Taylor, P. Tsai, N. van Rossum, A. Shah, A. D. Stepanov, D. A. Sutherland, T. R. Weber, U. Shumlak, and H. S. McLean, “Plasma pressure profiles in a sheared-flow-stabilized Z-pinch,” *Physics of Plasmas* **31**, 072503 (2024), https://pubs.aip.org/aip/pop/article-pdf/doi/10.1063/5.0209351/20027284/072503_1_5.0209351.pdf.

- ⁵⁶M. G. Haines and M. Coppins, “Universal diagram for regimes of Z-pinch stability,” *Phys. Rev. Lett.* **66**, 1462–1465 (1991).
- ⁵⁷D. D. Ryutov, M. S. Derzon, and M. K. Matzen, “The physics of fast Z pinches,” *Rev. Mod. Phys.* **72**, 167–223 (2000).
- ⁵⁸D. D. Ryutov, “Characterizing the Plasmas of Dense Z-Pinches,” *IEEE Transactions on Plasma Science* **43**, 2363–2384 (2015).
- ⁵⁹C. N. Lashmore-Davies and T. J. Martin, “Electrostatic instabilities driven by an electric current perpendicular to a magnetic field,” *Nuclear Fusion* **13**, 193 (1973).
- ⁶⁰G. V. Vogman and J. H. Hammer, “Complete quasilinear model for the acceleration-driven lower hybrid drift instability and a computational assessment of its validity,” *Phys. Rev. E* **110**, 025201 (2024).
- ⁶¹Y. Zhou and P. M. Bellan, “Two-stream instability with a growth rate insensitive to collisions in a dissipative plasma jet,” *Physics of Plasmas* **30**, 052101 (2023), https://pubs.aip.org/aip/pop/article-pdf/doi/10.1063/5.0146806/17177530/052101_1_5.0146806.pdf.
- ⁶²V. I. Arnold, *Mathematical Methods of Classical Mechanics*, Graduate Texts in Mathematics (Springer New York, 2013).
- ⁶³G. O. Spies, “Visco-resistive stabilization of kinks with short wavelengths along an elliptic magnetic stagnation line,” *Plasma Physics and Controlled Fusion* **30**, 1025 (1988).
- ⁶⁴A. H. Glasser and R. A. Nebel, “The stability of the high-density z-pinch,” *AIP Conference Proceedings* **195**, 226–235 (1989), https://pubs.aip.org/aip/acp/article-pdf/195/1/226/11529489/226_1_online.pdf.
- ⁶⁵F. L. Cochran and A. E. Robson, “Viscoresistive stabilization of the Z pinch,” *Physics of Fluids B: Plasma Physics* **5**, 2905–2908 (1993), https://pubs.aip.org/aip/pfb/article-pdf/5/8/2905/12299687/2905_1_online.pdf.
- ⁶⁶P. M. Cox, “Resistive and viscous effects on z-pinch stability,” *Plasma Physics and Controlled Fusion* **32**, 553 (1990).
- ⁶⁷S. Cappello and D. F. Escande, “Bifurcation in viscoresistive mhd: The hartmann number and the reversed field pinch,” *Phys. Rev. Lett.* **85**, 3838–3841 (2000).
- ⁶⁸Z. Yoshida and A. Hasegawa, “Anomalous transports associated with the helicity transport in a plasma,” *Physics of Fluids B: Plasma Physics* **3**, 3059–3064 (1991), https://pubs.aip.org/aip/pfb/article-pdf/3/11/3059/12317555/3059_1_online.pdf.

- ⁶⁹J. M. Finn, “Hyperresistivity due to viscous tearing mode turbulence,” *Physics of Plasmas* **12**, 092313 (2005), https://pubs.aip.org/aip/pop/article-pdf/doi/10.1063/1.2048887/16075195/092313_1_online.pdf.
- ⁷⁰B. K. Shivamoggi, “Hall magnetohydrodynamics near an x-type magnetic neutral line,” *Europhysics Letters* **85**, 25001 (2009).
- ⁷¹A. Stanier, W. Daughton, L. Chacón, H. Karimabadi, J. Ng, Y.-M. Huang, A. Hakim, and A. Bhattacharjee, “Role of ion kinetic physics in the interaction of magnetic flux ropes,” *Phys. Rev. Lett.* **115**, 175004 (2015).
- ⁷²X. Fan, P. H. Diamond, and L. Chacón, “Spontaneous transport barriers quench turbulent resistivity in two-dimensional magnetohydrodynamics,” *Phys. Rev. E* **99**, 041201 (2019).
- ⁷³There is in fact a singularity in the limit $\mathfrak{B}_\alpha \rightarrow \infty$, in which the width of the layer about the axis goes to zero. Within this layer, the cyclotron and betatron current densities diverge to $\pm\infty$.
- ⁷⁴J. D. Lawson, *Particle Beams and Plasmas*, Lectures Given in the Academic Training Programme of CERN, 1973-1974 No. No. 9 (European Organization for Nuclear Research, 1976).
- ⁷⁵A. Marinelli, E. Hemsing, and J. B. Rosenzweig, “Three dimensional analysis of longitudinal plasma oscillations in a thermal relativistic electron beam,” *Physics of Plasmas* **18**, 103105 (2011), https://pubs.aip.org/aip/pop/article-pdf/doi/10.1063/1.3638139/13612933/103105_1_online.pdf.
- ⁷⁶G. V. Vogman, J. H. Hammer, U. Shumlak, and W. A. Farmer, “Two-fluid and kinetic transport physics of Kelvin–Helmholtz instabilities in nonuniform low-beta plasmas,” *Physics of Plasmas* **27**, 102109 (2020), https://pubs.aip.org/aip/pop/article-pdf/doi/10.1063/5.0014489/15924640/102109_1_online.pdf.
- ⁷⁷V. I. Geyko, J. R. Angus, and M. A. Dorf, “Gyrokinetic and extended-MHD simulations of a flow shear stabilized Z-pinch experiment,” *Physics of Plasmas* **28**, 052113 (2021), https://pubs.aip.org/aip/pop/article-pdf/doi/10.1063/5.0037506/13917819/052113_1_online.pdf.
- ⁷⁸E. T. Meier and U. Shumlak, “Development of five-moment two-fluid modeling for Z-pinch physics,” *Physics of Plasmas* **28**, 092512 (2021), https://pubs.aip.org/aip/pop/article-pdf/doi/10.1063/5.0058420/13420598/092512_1_online.pdf.